Chem Soc Rev

REVIEW ARTICLE

View Article Online
View Journal

Cite this: DOI: 10.1039/d0cs01568g

Single molecule fluorescence imaging of nanoconfinement in porous materials†

Bin Dong, *[a] Nourhan Mansour,[a] Teng-Xiang Huang,[a] Wenyu Huang *[bc] and Ning Fang*[a]

Received 17th December 2020

DOI: 10.1039/d0cs01568g

rsc.li/chem-soc-rev

This review covers recent progress in using single molecule fluorescence microscopy imaging to understand the nanoconfinement in porous materials. The single molecule approach unveils the static and dynamic heterogeneities from seemingly equal molecules by removing the ensemble averaging effect. Physicochemical processes including mass transport, surface adsorption/desorption, and chemical conversions within the confined space inside porous materials have been studied at nanometer spatial resolution, at the single nanopore level, with millisecond temporal resolution, and under real chemical reaction conditions. Understanding these physicochemical processes provides the ability to quantitatively measure the inhomogeneities of nanoconfinement effects from the confining properties, including morphologies, spatial arrangement, and trapping domains. Prospects and limitations of current single molecule imaging studies on nanoconfinement are also discussed.

1. Introduction

Porous materials, in which the guest molecules are encapsulated in the nanoscale confined space within the porous network, have been used in various applications, such as catalysis,[1,2] biological and environmental sensing,[3,4] chromatography,[5,6] energy generation and storage,[7–10] selective sequestration of contaminants,[11,12] and drug delivery.[13,14] Understanding the nanoconfinement in porous materials has been gaining a lot of interest because confined molecules can fundamentally change their chemical and physical properties compared to those in bulk conditions.[15–17]

In chemical reactions, nanoconfinement can result in changes in specific reaction pathways by tuning geometrical constraints, selective adsorption, and potential energy surface, thus eventually influencing activity and selectivity.[18,19] For instance, the confinement of molecules has enabled the

[a] Department of Chemistry, Georgia State University, Atlanta, Georgia 30303, USA. E-mail: bdong@gsu.edu, nfang@gsu.edu
[b] Department of Chemistry, Iowa State University, Ames, Iowa 50011, USA. E-mail: whuang@iastate.edu
[c] Ames Laboratory, U.S. Department of Energy, Ames, Iowa 50011, USA

† Part of the themed collection of Chemical Society Reviews on Nanoconfinement.

Bin Dong

Bin Dong received his BS in Chemistry from the Xiamen University, China, in 2011 and did his PhD work with Prof. Ning Fang and Prof. Wenyu Huang in Analytical Chemistry at Iowa State University. In 2015, he joined Prof. Ning Fang's group at Georgia State University for postdoctoral research in experimental physical and analytical chemistry. His current research interests are in developing advanced optical imaging methods and applying them for chemical and biophysical studies at the single molecule level and nanoscale.

Nourhan Mansour

Nourhan Mansour received her BS in Chemistry from the American University in Cairo, Egypt in 2010 and completed graduate courses in Nanotechnology. Currently she is a graduate student under the supervision of Prof. Ning Fang in the Department of Chemistry at Georgia State University. Her research focuses on single-molecule and single-particle imaging of nanoconfinement in heterogeneous catalysis.

synthesis of selected amino acids and sugars, the stabilization of polymers such as RNA and polyglycine, and the restoration of misfolded proteins to their native structures.[15,20] On the other hand, the mass transport of molecules under nanoconfinement is orders of magnitude slower than that in bulk liquids.[21] The mass transport and the accessibility of reactant molecules in porous materials can greatly influence their catalytic activities or the selectivities of the final products. In many reactions, it is of great importance to understand the diffusion of reactants into the porous material because the efficiency in such applications mainly depends on the penetration and partitioning behaviors of the molecules, which are strongly affected by the considerably enhanced steric and electrostatic interactions within the confined space.

Porous materials possess complicated structural features (*e.g.*, spatial arrangement, types, morphologies, and inhomogeneity of confined space) and physicochemical properties (*e.g.*, viscosity, hydrophobicity, and electronic charges) differing in their effects of nanoconfinement on confined chemical dynamics. For the rational design and synthesis of porous materials with improved performance, one needs quantitative correlations between the properties of nanoconfinement and the corresponding chemical dynamics, ideally obtained under realistic conditions. High-resolution electron microscopy, such as scanning transmission electron microscopy (STEM) and scanning tunneling microscopy (STM), has an atomic level spatial resolution but requires low-pressure conditions and/or conductive surfaces. Ensemble methods such as optical microscopy and spectroscopy, neutron scattering, and pulsed-field gradient nuclear magnetic resonance (NMR) spectroscopy can provide averaged information on pore morphology, pore integrity, pore environmental chemistry, *etc.* However, they lack the sensitivity down to the single molecule level and are unable to resolve the issue of inhomogeneity of nanoconfinement in complex porous materials. Neither electron microscopy nor ensemble characterization methods can directly access molecular chemical dynamics under nanoconfinement in porous materials.

In recent years, the development of single molecule fluorescence (SMF) imaging has brought new insights into biophysical studies and chemical measurements. For example, SMF imaging has been applied to investigate heterogeneous catalysis on solid catalysts for unveiling the hidden inhomogeneities in catalytic dynamics and stabilities of different surface features within single catalysts as well as among individual catalysts.[22–25] SMF imaging can reveal static and dynamic heterogeneities from seemingly equal molecules by removing the ensemble averaging effect at nanometer spatial resolution, millisecond temporal resolution, and under realistic reaction conditions. The recovered static positions and dynamic trajectories of individual molecules in SMF imaging enable one to unveil the features of the local environment, including morphologies, spatial arrangement, and trapping domains, and determine the dynamic behaviors of targeted molecules or objects such as diffusion rates and adsorption/desorption kinetics. By utilizing fluorogenic reactions,

Teng-Xiang Huang

Teng-Xiang Huang received his BS in Chemistry from the Xiamen University, China, in 2011 and did his PhD work with Prof. Bin Ren in Physical Chemistry at Xiamen University. In 2019, he joined Prof. Ning Fang's group at Georgia State University for postdoctoral research in experimental physical and analytical chemistry. His current research focuses on the utilization of advanced spectroscopy and optical imaging methods to study the physical and chemical processes on surfaces and interfaces at the single molecule level and nanoscale.

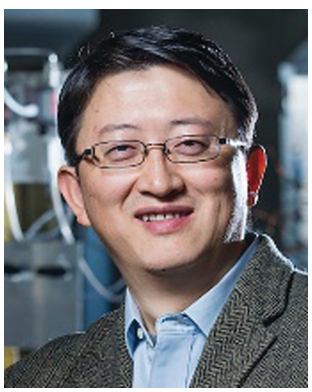

Wenyu Huang

Professor Wenyu Huang received his BS in Chemistry from Nanjing University, China, in 2000. After receiving his MS in 2002 also from Nanjing University, he started his PhD research with Professor Mostafa A. El-Sayed at Georgia Institute of Technology and received his PhD in 2007. Dr Huang then began postdoctoral research with Professor Gabor A. Somorjai and Professor Peidong Yang at University of California, Berkeley and Lawrence Berkeley National Laboratory in August 2007. He joined the faculty at Iowa State University in August 2011. His present research interest involves nanomaterials, heterogeneous catalysis, and polymer upcycling.

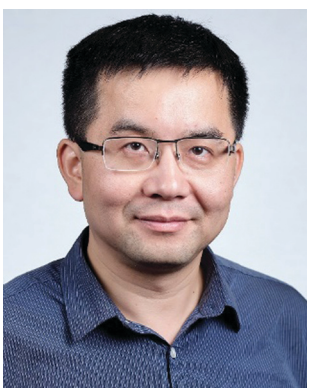

Ning Fang

Ning Fang received his BS in Chemistry from Xiamen University, China in 1998 and his PhD from the University of British Columbia, Canada with Prof. David Chen in 2006. He did his postdoctoral research at Iowa State University and USDOE Ames Laboratory with Prof. Edward Yeung from 2006 to 2008. He became an Assistant Professor at Iowa State University in 2008. He moved to Georgia State University to become an Associate Professor in 2015, then a Full Professor in 2021. His research aims to open new frontiers in chemical and biological discovery through the development of optical imaging platforms.

SMF imaging also enables the monitoring of single molecule reaction dynamics by counting individual turn-over events, deconvolution of individual kinetic steps, and revealing hidden reaction dynamic inhomogeneities in both spatial and temporal domains.

Over the last decade, numerous SMF imaging studies, taking advantage of high spatial and temporal resolution, have been conducted to acquire direct experimental measurements and achieve a quantitative understanding of the nanoconfinement at the single molecule and single nanopore levels. This review surveys the application of single molecule fluorescence imaging in understanding the effects of nanoconfinement in porous materials, with a focus on the dynamic mass transport behaviours of individual molecules within porous materials of various structural features and chemical environments as well as the nanoconfinement effects on heterogeneous catalysis, including catalyst effectiveness and reaction dynamics within well-defined structures. Further studies on the review articles on single molecule fluorescence imaging of chemical dynamics are strongly encouraged.[24–32]

2. Mass transport in a confined space

Porous materials have gained a lot of interest due to their large surface area, controllable structure, and ease of preparation.[20] The porous structures act as pathways that can limit or enhance the mass transport of the incorporated molecules. Examples of the most commonly employed self-organized nanostructured materials with 1D pathways include mesoporous silica or metal oxides, lyotropic and thermotropic liquid crystals (LCs), microporous coordination polymers (MCPs), and block copolymers (BCPs). These nanostructured materials have the ability to selectively transport particular chemical species. The partitioning of guest molecules and the mass transport within the nanoscale domain affects the transport rate and the selectivity of such models. These nanostructures may have different barriers that confine the molecular motion in one or more dimensions. Moreover, the mass transport could be affected by molecular-level processes such as steric, chemical, and electrostatic interactions between the guest molecules and the nanostructured medium. Therefore, it is important to achieve a better understanding of the mechanism of mass transport in such a confined space to design optimized materials for specific applications such as chromatographic separation.[30] So far, mass transport in a confined space has been mainly studied using ensemble measurements. For instance, various studies have focused on the subject of molecular diffusion in porous materials by employing various methods such as fluorescence recovery after photobleaching (FRAP), infrared (IR) spectroscopy, pulsed-field gradient nuclear magnetic resonance (NMR), and quasi-elastic neutron scattering. In recent years, single molecule spectroscopy (SMS) has been developed to directly monitor the behaviors of individual molecules in a confined space, thus enabling spatial and temporal visualization and a better understanding of heterogeneous molecular dynamics under diverse nanoconfinements in complex porous materials.[33]

Two different SMS techniques can be used to study the diffusion of fluorescent dye molecules. The first method is fluorescence correlation spectroscopy (FCS), which uses a microscopy apparatus to observe the diffusion of individual molecules entering and exiting a well-defined small detection volume. The fluctuations of the detected fluorescence intensity in time $I(t)$ can be statistically analyzed to extract the diffusion coefficients.[33] The limitation of this method is that, in order to obtain a diffusion coefficient, it requires the fitting of the intensity autocorrelation function with a theoretical expression derived from a model of the diffusion process. Moreover, the temporal and spatial information of individual molecules is not accessible in this method.[33] The second method is directly analyzing a series of fluorescence microscopy images, *i.e.*, movies, of diluted fluorescent molecules. In those movies/images, the fluorescence of individual dye molecules is imaged on cameras in many frames as diffraction-limited patterns that can be tracked and analyzed; thus, this method is known as single molecule tracking (SMT). SMT does not require a model assumption and allows us to directly characterize the molecular motion in space and time to observe various diffusion behaviors from analyzing the reconstructed trajectories. This method is not sensitive for fast processes in comparison to FCS and requires a sufficient acquisition time ($>$ms) for obtaining single molecule images with a sufficient signal to noise ratio (SNR). Both methods have their own pros and cons,[34–36] and here we will mainly cover studies on SMT in porous materials. SMT can be used to investigate single molecules diffusing in porous materials by revealing the presence of a distinct diffusion behavior of individual molecules and a heterogeneous behavior in the trajectory when they are trapped in a nanometer-sized confined space. SMT also allows us to observe deviations in the distribution of step sizes which could be due to adsorption sites and molecular-size barriers present in the material or anisotropy in the material structure.[33]

2.1. Overview of single molecule tracking in porous materials

To achieve single molecule detection in porous materials, the guest molecules (*i.e.*, fluorescence probes) are loaded into the porous structures with very low concentrations at the nano- or pico-molar level so that it is possible to resolve individual molecules spatially. There are several ways to incorporate fluorescent molecules into porous materials, including entrapping the guest molecules inside the porous materials during synthesis or incubating the guest molecules with the host material for a particular time period. Typically, sequences of SMF images (Fig. 1A) are recorded with a wide-field imaging setup. A laser beam is used to illuminate a certain spot on the sample to excite the probe molecules causing them to fluoresce. The fluorescence photons are then collected by an objective and imaged onto a highly sensitive detector such as the electron-multiplying charge-coupled device (EMCCD).

Localize and track molecular positions with nanometer precision. The actual sizes of fluorescent probe molecules are typically only a few nanometers; however, their fluorescence images are much larger, usually a few hundreds of nanometers,

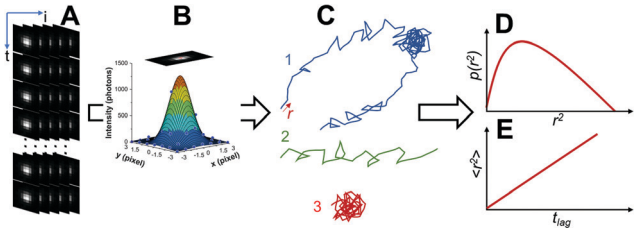

Fig. 1 Single molecule tracking in porous materials. (A) Multiple time sequences of single molecule fluorescence images. (B) Localize the center positions of fluorescent molecules with nanometer precision using PSF (*e.g.*, 2D elliptical Gaussian) fitting image intensity distribution. (C) Recovered single molecule trajectories. (D) Characterize MSD by fitting the distribution of step sizes or displacements (r) with PDF. (E) Determine the diffusion coefficient by fitting MSD *versus* lag time.

which is approximately one-half of the light wavelength. This effect can be described by the point-spread function (PSF) in light microscopes. Although the true shapes and sizes of the fluorescent probe molecules are not available in fluorescence microscopy imaging, their center positions (x_0, y_0) can be accurately determined by fitting the intensity distributions ($I(x,y)$) of these single molecule images with the PSF (Fig. 1B). The Gaussian functions are often used as a suitable approximation of the PSF in fitting the intensity distributions.[37]

$$I(x,y) = A \times \exp\left(-\left(\frac{(x-x_0)^2}{2S_x^2}+\frac{(y-y_0)^2}{2S_y^2}\right)\right) \quad (1)$$

The accuracy in localizing the center positions depends on the collected photons of single molecule images and can be calculated using eqn (2),[37] where S_j is the standard deviation of the single molecule fluorescence image, a is the pixel size of the camera, N is the collected photon number from single fluorescent molecules, and b is the fluorescence background noise level.

$$\sigma_j = \sqrt{\frac{S_j^2}{N}+\frac{a^2/12}{N}+\frac{8\pi S_j^4 b^2}{a^2 N^2}} \quad (2)$$

With sufficient photons collected and low fluorescence background noise, the localization precision can be as high as 1 nm.[38] Trajectories of the movement of fluorescent molecules (Fig. 1C) can be reconstructed from precisely localized positions as described above, thus enabling one to directly visualize the dynamic mass transport behaviors of confined guest molecules in porous materials.

Quantify diffusion behaviors from molecular trajectories. After obtaining the molecular positions in time series (*i.e.*, trajectories), one can quantify the mass transport properties in porous materials using statistical methods, for instance, mean squared displacement (MSD) analysis. The MSD analysis is applied by taking the difference between two molecular positions along with the trajectory that is separated by a certain time, *i.e.*, lag time t_{lag}. The step sizes or displacements (r^2) at a certain lag time are first calculated from the trajectories and their mean values ($\langle r^2\rangle$) are then plotted *versus* the lag time. Alternatively, one can perform the histogram distribution analysis of the obtained step sizes. The obtained histogram distribution could be fitted with a radial probability density function (PDF)[39] to extract the characteristic mean squared displacement (Fig. 1D).

$$p(r^2,t)\cdot \mathrm{d}r^2 = \frac{1}{\pi\langle {r_{(t)}}^2\rangle}\exp\left(\frac{-{r_{(t)}}^2}{\langle {r_{(t)}}^2\rangle+\sigma^2}\right)2\pi r\cdot \mathrm{d}r^2 \quad (3)$$

One can fit the $\langle r^2\rangle$–t_{lag} relationship to extract the kinetic parameter in mass transport, *i.e.*, diffusion coefficient, using the Einstein–Smoluchowski equation for random diffusion in n dimensions (Fig. 1E).

$$\langle r^2\rangle = 2nDt_{lag} \quad (4)$$

Furthermore, the measured diffusion coefficient can also be used to determine the apparent viscosity (η) of the medium inside the nanoconfinement using eqn (5),[40] where k_B is the Boltzmann constant, T is the temperature, and r_0 is the size of fluorescent probe molecules.

$$D = \frac{k_B T}{2n\pi\eta r_0} \quad (5)$$

Uncover heterogeneous diffusion behaviors. Inhomogeneous diffusion dynamics can be seen either among or within individual trajectories. In the latter case, one may directly observe distinct regions of different diffusion behaviors as they spread out in space. Molecular trajectories within these regions can be quantified separately to examine their differences in diffusion coefficients and properties of the local nanoconfinement such as viscosity. However, this may not always be true where one cannot readily tell the existence of such heterogeneous regimes within molecular trajectories. Such hidden heterogeneous diffusion behaviors can be recovered from the displacement analysis, where a single component PDF cannot fully describe the distribution of displacement. The multicomponent PDF with distinct diffusion coefficients can then be used to describe the heterogeneous diffusion behaviors of molecules.[14]

$$p(r^2,t)\cdot \mathrm{d}r^2 = \sum_1^i c_i \frac{1}{\pi\langle {r_{i(t)}}^2\rangle}\exp\left(\frac{-{r_{(t)}}^2}{\langle {r_{i(t)}}^2\rangle+\sigma^2}\right)2\pi r\cdot \mathrm{d}r^2 \quad (6)$$

Based on the measurement results, the mass transport of fluorescent probe molecules in the nanopores can be categorized into several sub-groups such as fast, moderate, and slow diffusion. Such results usually suggest that the mass transport of fluorescent probe molecules cannot be described simply as one Brownian motion, but rather as a combination of diffusion and adsorption behaviors associated with variable local nanoconfinement environments in porous materials.

Inhomogeneities among individual molecular trajectories are also often observed. As shown in Fig. 1C, three types of molecular trajectories can be identified, namely, mobile, immobile and hybrid modes. These distinct trajectories can be quantitatively analyzed separately, and the determined diffusion coefficients, in combination with nanometer-precision positions, can be used to reconstruct high-spatial-resolution mapping showing heterogeneous regimes of diffusivity in porous materials.

Three-dimensional single molecule tracking. By extending to three-dimensional (3D) single molecule localization, additional vital information can be obtained, including the visualization of structures or motions extending in the axial direction and a better understanding of complex systems. 3D super-resolution images and 3D tracking can be achieved by interferometric detection, multiple focal plane imaging, and point-spread-function engineering.[41] For example, Zhao *et al.* employed the 3D single-particle tracking method to monitor the microscopic motion of 100 nm nanoparticles in cylindrical alumina nanopores (~3 μm in diameter) with a z-span as large as several micrometers.[42] This study revealed that particles could be retained inside the pores over an extended period due to either increased solvent viscosity or increased pore wall affinity, demonstrating the ability to differentiate different mechanisms for slow diffusion in confined environments.

2.2. Mass transport and local structure of nanoconfinement

Mesoporous materials synthesized through surfactant self-assembly and framework building blocks can be tuned to adopt a variety of structures, which made them widely employed in various applications. The local structure of the confined environment can greatly influence molecular diffusion. Distinct regimes or modes of molecular diffusion could occur within the pore networks, which may arise from structural heterogeneities of the materials such as slight variations of the pore diameter. The viscosity of the medium in the confinement also increases due to stronger molecular interactions. Therefore, it is important to understand the molecular movement inside the porous materials and how the local structures, such as domains and defects, influence the movement of confined molecules. Optical and transmission electron microscopies fail to directly image the mesoporous structure or provide dynamic information on molecular diffusion. The high spatial and temporal resolution of SMT enables one to obtain this information and provide insights into the heterogeneity and details of molecular diffusion as well as the structure of the porous host.

Spatially resolve heterogeneous nanoconfinement. SMF microscopy has been used to assess, quantify, and map heterogeneities in local diffusion properties within complex porous materials. For instance, Weckhuysen *et al.* used SMF microscopy to study single molecule diffusion inside a complex network of micropores (internal diameter <2 nm), mesopores (2–50 nm), and macropores (>50 nm) in real-life fluid catalytic cracking (FCC) particles.[43] FCC particles are used for producing half of the gasoline worldwide because they are the catalysts for one of the main conversion processes in the oil refinery. In this work, they studied the diffusion of the feedstock-like probe molecule, *i.e.*, *N*,*N*′-bis(2,6-dimethyl phenyl)-perylene-3,4,9,10-tetracarboxylic diimide (PDI), within the complex pores of micrometer-sized FCC particles (~20 μm in diameter). The recorded movies of single fluorescent molecules allowed the classification of their movement through the porous networks into three different states: immobile, mobile, and hybrid (Fig. 2A). The average apparent diffusion coefficients of each type (Fig. 2B) were measured to reveal such diffusive heterogeneity across the entire

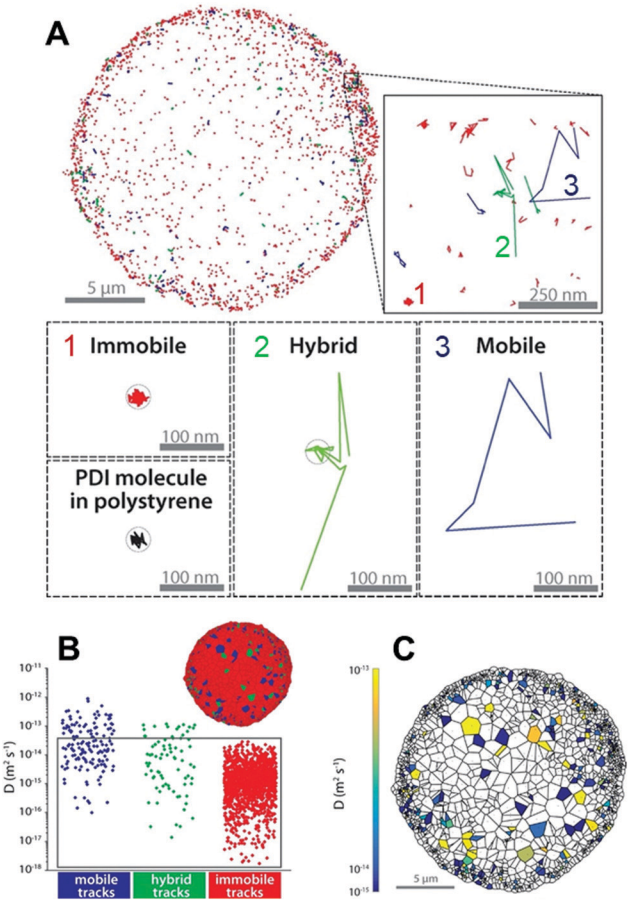

Fig. 2 SMF imaging of heterogeneous diffusion in the pore network of FCC particles. (A) Super-localization mapping of the diffusion of PDI molecules in an FCC particle. (B) Diffusion coefficients of each type of track. The gray rectangle includes diffusion coefficients falling within the localization uncertainty of the single molecule analysis. The inset Voronoi diagram shows the spatial distribution of each track type. (C) Diagram showing localized diffusion coefficients in the middle cross section of the FCC particle. The color of each area indicates the diffusion coefficient, with areas around immobile tracks being white. Figures are adapted from ref. 43 with permission. Copyright 2017 American Chemical Society.

FCC particle (Fig. 2C). This study shows the heterogeneity of the local pore structure and how it influences the molecular transport.[43]

To determine the diffusion behaviors of analytes and obtain better separation efficiency in high performance separation techniques, *e.g.*, reversed phase liquid chromatography (RPLC) using porous particles, it is important to understand the time scale of processes responsible for analyte retention in the stationary phase. Harris *et al.* used SMF imaging to observe the transport of individual molecules within C_{18}-modified porous silica particles (Fig. 3).[5] This study focused on characterizing intraparticle molecular transport when individual molecules visit C_{18}-modified porous silica particles. The residence times and diffusion rates of octadecyl rhodamine B (R18), as well as its spatial distribution within the porous silica particles, were extracted from SMT experiments. The recorded molecular trajectories were divided into moving (N_m) and stationary (stuck, N_S) time segments.

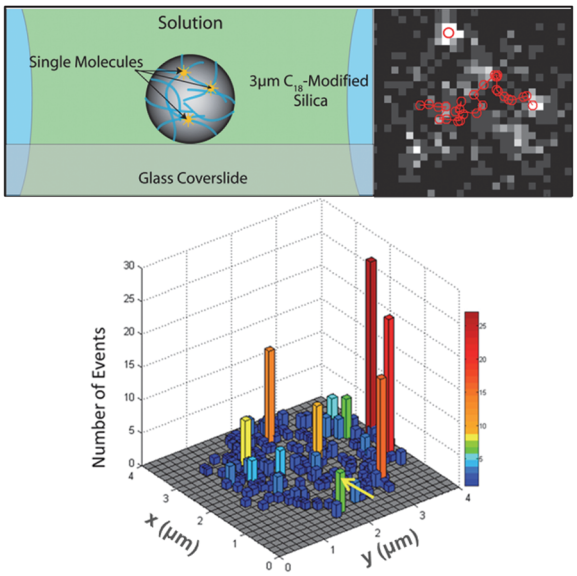

Fig. 3 SMF imaging of R18 molecules diffusing in C_{18}-modified porous silica particles. Schematic view (top left), single molecule images of R18 dye molecules (top right), and a 2-D map of stuck events at resolved sites (bottom) where color bars describe the number of events. Figures are adapted from ref. 5 with permission. Copyright 2013 American Chemical Society.

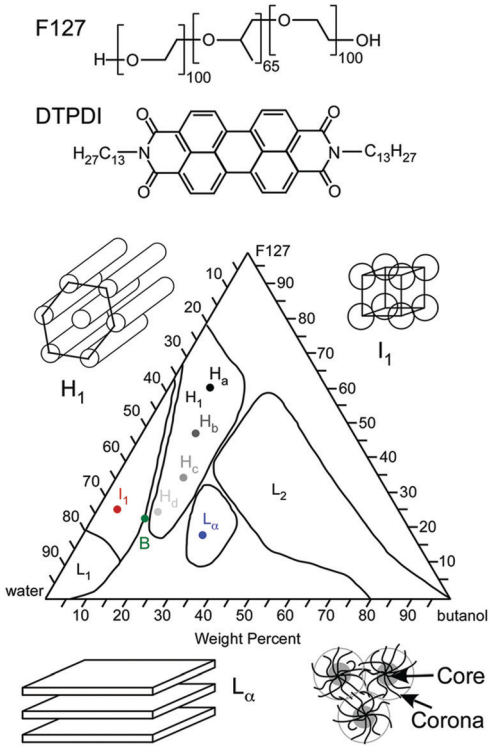

Fig. 4 Phase diagram for F127/water/butanol mixtures. Shown are the normal hexagonal (H_1), isotropic (I_1), and lamellar (L_α) regions investigated, along with the normal (L_1) and reverse (L_2) micellar regions. The filled circles appended to H_1, I_1, and L_α regions depict the samples prepared and characterized. The diagrams at the upper left, upper right, and lower left show simple models for assembly of copolymer molecules in each phase. The diagram at the lower right depicts the core and corona regions of cylindrical and spherical micelles. Figures are adapted from ref. 50 with permission. Copyright 2011 American Chemical Society.

The stationary molecules represent the strong adsorption that would lead to peak tailing in chromatographic elution with a higher residence time. These strong retention sites at the interfacial surface of solid materials such as defects of available silanols are often unavoidable during the materials synthesis and fabrication process, which can interact with analyte molecules thorough interfacial forces like hydrogen bonding and electrostatic interactions.[5,44–46] SMF imaging enables the understanding of the separation mechanism at the molecular, nanoscale level and can inspire future work in modifying stationary phases to improve the separation performance by both synthetic methods and theoretical simulations, for example, designing strategies to reduce silanol prevalence.[47–49] Furthermore, the calculated capacity factor, $k' = N_S/N_m \sim 490$, suggested that R18 molecules spend only 0.2% of their time in the mobile phase. In other words, almost all of the intraparticle transport occurs in the form of surface diffusion on the C_{18}-modified silica stationary phase.

Spatial arrangement, types, and morphologies of nanoconfinement. Heterogeneous nanoconfinement can be created by changing the spatial arrangement of a variety of pore structures. SMT has also been employed to show how the pore arrangements or types cause different confinement effects on molecular behaviors.

Higgins *et al.* investigated the diffusion of the hydrophobic perylene diimide (DTPDI) dye molecules within the mesophase structures, *i.e.*, hexagonal, lamellar, and cubic regions, of Pluronic F127 gels that are a series of dye-doped F127/water/butanol mixtures (Fig. 4).[50] In the hexagonally arranged cylindrical gels, DTPDI molecules exhibited distinct 1D diffusion within the viscous and hydrophobic micelle cores. In comparison, DTPDI molecules in the lamellar and cubic mesophases exhibited isotropic 2D and 3D diffusion behaviors. The diffusion in the cubic regions were found to be much slower due to long-term confinement of the dye molecules in the micelle core. A bimodal diffusion coefficient distribution was observed: the slow diffusion reflected the 1D motion in the micelle core, while the faster component reflected the partitioning or 3D diffusion in the interconnected micelle coronas. These results provide vital information for understanding the individual roles played by the micelle core and corona in governing molecular diffusion.

Bräuchle *et al.* employed SMF microscopy to track strongly fluorescent terrylene diimide (TDI) dye molecules inside mesoporous silica channel systems.[51,52] The mesoporous silica channel system was prepared as thin films *via* cooperative self-assembly of surfactant molecules with polymerizable silicate species, resulting in three different samples: a single pure hexagonal mesophase, a single pure lamellar mesophase, and the third sample in which the two mesophases coexisted. The molecules in the lamellar phase maintained a constant orientation perpendicular to the glass substrate and normal to the silica planes during diffusion because of the strong interactions of the dye molecules with the template molecules, whereas the molecules in the hexagonal

phase diffused faster and reoriented constantly, indicating much weaker interactions with the template than in the lamellar phase. Their results demonstrated that different topologies strongly influenced the diffusion of the molecules inside the pores. This approach provides a detailed picture of the structure and connectivity of different nanopore systems and how they would influence molecular diffusion.[51] In another study, the same group investigated the influence of pore size on molecular diffusion in cast silica xerogels and on spatial heterogeneities.[53] Two types of monolithic silica gels with different porosities were doped with the streptocyanine dye. The first type of gel had a pore size similar to the size of the dye molecule (3 nm mesopore), while the other had a bigger pore size (22 nm mesopore). The dye molecules were found to be largely (80%) trapped in regions of narrower pores (diameter of 50–200 nm), while the wider pores had fewer physical traps. Statistical analysis of the single molecule trajectories revealed that the gel with a wider pore allowed the dye molecules to diffuse freely and had a higher diffusion coefficient compared to the gel with smaller pores. This shows the significance of the pronounced microscopic inhomogeneities and the distribution of diffusion coefficients due to the difference in pore size and the local structure.[53]

Structural domains and defects in nanoconfinement. Studies have also been conducted to obtain information on the nanoconfinement environment such as the domain size and how it affects the molecular transport.

Lately, both fluorescence recovery after photobleaching (FRAP) and SMT measurements have been used to provide complementary information on molecular diffusion in porous materials and how the domain size of the nanoconfinement environment affects the molecular transport. Ito *et al.* employed both techniques (Fig. 5) and obtained a direct comparison of the molecular diffusion information within identical regions of a cylinder-forming polystyrene–poly(ethylene oxide) diblock copolymer (PS-*b*-PEO) film ($\sim$4 μm thick) with aligned cylindrical PEO microdomains containing 10 μM sulforhodamine B (SRB).[54] FRAP was used to study the ensemble diffusion behavior of SRB in the domains at the microlevel, while SMT was used to study the diffusion of individual SRB molecules at the nanoscale. The obtained average diffusion direction and coefficient for the florescent molecule inside the cylindrical domain were similar for both methods. FRAP measurements assisted in studying the longer range diffusion behavior at a $\geq$100 μm microdomain length, while SMT measurements were used to assess the distribution of mass transport properties of individual molecules. FRAP offered information on the microdomain morphology, such as its effective length, orientation, and dimensionality. SMT also provided information on the dimensionality and orientation of individual microdomains plus single molecule diffusion coefficients. By applying both methods on identical sample areas, they were able to minimize the influence of the compositional and morphological heterogeneity on accurate mass transport measurements, therefore permitting a direct comparison of ensemble and single molecule diffusion behaviors.

TDI dye molecules have also been incorporated into CTAB-templated hexagonal mesoporous silica films containing highly

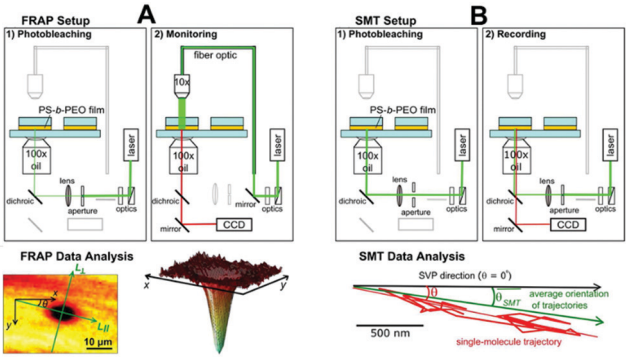

Fig. 5 Experimental setups for FRAP and SMT measurements. (A) Top: For FRAP measurements, a circular region in a PS-*b*-PEO film was first photobleached using an intense laser pulse. Subsequently, the fluorescence was imaged by irradiating the sample with attenuated laser light from the top. Bottom: A representative fluorescence image of a photobleached region in the FRAP experiment. (B) Top: All SMT data were recorded (right) under broad laser illumination after the wider observation area was further photobleached (left) by more intense laser light. Bottom: A typical 1D single molecule trajectory (red) and its best-fit line using orthogonal regression methods. Here, θ represents the tilt angle (red) of the single trajectory with respect to the solvent-vapor penetration direction ($-90^\circ \leq \theta \leq 90^\circ$) while θ_{SMT} depicts the average trajectory orientation from all 1D trajectories found in each set of SMT data (green). Figures are adapted from ref. 54 with permission. Copyright 2015 American Chemical Society.

structured domains as a host (Fig. 6).[55] The diffusional and orientational behaviors of the TDI molecules were monitored by polarization modulated confocal microscopy. By examining different atmospheric conditions, it was shown that the TDI molecules were free to diffuse linearly along with the pores in chloroform, but they were immobile in the air (Fig. 6A and B). Furthermore, the transition dipole moment did not change its orientation along the trajectories (Fig. 6C), suggesting the host having highly linear channels with rare defects. Moreover, dead ends and connections between the adjacent pores were detected from the single molecule trajectories. The data also showed that the overall diffusion of the dye molecules could not be described by a 1D random walk, but it was more complicated because the diffusion was occasionally interrupted by temporary entrapment of molecules at the adsorption sites. Therefore, the investigation of the translational and orientational dynamics *via* SMF techniques with very a high positioning accuracy (down to 2–3 nm) gives structural as well as dynamic information, and it is essential for enhancing the performance of mesoporous solids for applications in separation, catalysis, chemical sensors, and host–guest chemistry.[55]

2.3 Mass transport and chemical environment of nanoconfinement

It has been observed that the chemical environment in which the guest molecules are confined has a great influence on their molecular diffusion. The capability of controlling guest molecules in the host materials can be greatly beneficial for a large variety of applications.

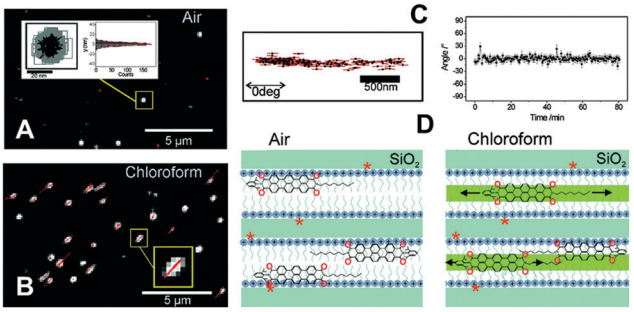

Fig. 6 Parallel orientation and diffusion of single TDI molecules in highly structured domains. Single TDI molecules embedded in parallel pores in air atmosphere (A) and in chloroform (B). (C) A single molecule trajectory of TDI molecules embedded in parallel pores in chloroform (left) and the calculated angular time trajectory of the same molecule (right). (D) Schematic of TDI molecules immobilized in the mesoporous material in air atmosphere (left) and diffusing in the mesoporous material in the presence of chloroform (right). The stars indicate the presence of active silanol groups. Figures are adapted from ref. 55 with permission. Copyright 2008 American Chemical Society.

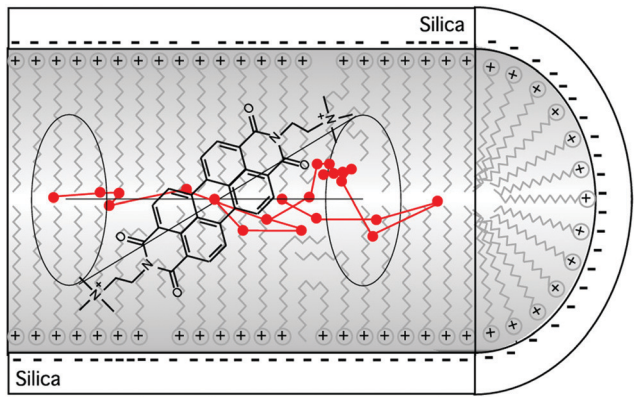

Fig. 7 Schematic view of mass transport of charged PDI molecules confined in mesoporous silica pores with nanometer sizes. Figures are adapted from ref. 20 with permission. Copyright 2020 American Chemical Society.

Viscosity. Wang *et al.* have developed a 3D single-particle localization technique to study how viscosity and the wall pore affinity influence molecular transport in confined environments.[42] The microscopic motion of carboxylated polystyrene nanoparticles in cylindrical alumina nanopores with a z-span as large as several micrometers was imaged for studying the effects of increased solvent viscosity and particle–surface interactions on diffusion in nanopores. This experiment showed that increasing the buffer viscosity slowed down the particle motion significantly throughout the entire pore structure (Fig. 8A), while increasing the pore wall affinity only slowed down the microscopic motion of the particles slightly (Fig. 8B), which is likely because the increased pore wall affinity only slowed down the particles at the wall. This was a good demonstration of 3D single particle tracking techniques for differentiating different factors in influencing molecular dynamics in confined environments.

Interfacial electrostatic force. The charges and electrostatic interactions between the host material and confined molecules have been shown to define the mass transport within porous materials.

A recent study by Higgins *et al.* investigated the effects of charges on mass transport in one-dimensional (1D) nanoscale pores of surfactant-templated mesoporous silica films.[20] In this work, polarization-dependent single molecule tracking was employed to observe the translational and rotational diffusion of perylene diimide (PDI) dyes of different lengths and charges inside the silica mesopores (Fig. 7). The acquired fluorescence videos revealed that the majority of the molecules exhibited 1D diffusion as well as highly polarized fluorescence, consistent with their orientational confinement. The acquired step size distributions were fitted with a model of the 1D Fick diffusion in the presence of finite localization precision. The two neutral PDIs had 20–100% larger average diffusion coefficients compared to the charged PDIs, which could be explained by the electrostatic interactions of charged PDIs with the oppositely charged sites on the cationic surfactant headgroups and deprotonated silanol sites on the pore walls. The longest uncharged PDI was found to be more confined than the other three shorter dyes. Since the dyes diffuse in a highly oriented state, the orientation confinement of the 1D diffusing dye molecules was evident by the strongly polarized emission. A subtle depolarization of the fluorescence represents the confined orientational wobbling of the molecules and allows the measurement of the wobbling motions and the lateral dimensions of the pathway that each dye molecule follows within the pore. It was found that cationic PDI explored more of the pore diameter as it produced a broader wobbling angle distribution compared to the others. The information on how the confined molecules interact with the surfactant filling the pores as well as on the pore surface is important to understand the mass transport within porous materials.[20]

Bräuchle *et al.* employed SMF techniques to study the orientational and spectral dynamics of single molecules in nanostructured host–guest materials.[56] Oxazine-1 dye molecules that were encapsulated tightly inside microporous AlPO4-5 crystals (a zeotype structure (artificial zeolites)) did not show any movement, while terrylenediimide (TDI) molecules inside the pores of a templated mesoporous silica (uncalcined M41S film) showed more orientational dynamics and interrupted movement supported by the fixed orientation of the molecule for a certain period of time. Those movement interruptions could be due to the interactions with the silica wall and the electrostatic interactions with the cationic template or at defect sites.

Hydrophobicity. The hydrophobicity of the pore structure is another key factor that influences molecular transport within the nanochannels. Recently Bein *et al.* functionalized the wall of mesoporous silica networks/films with alkyl molecules to study the diffusion behavior of single terrylene diimide (TDI) dye molecules using SMF microscopy.[57] The influence of functional-group polarity on the diffusion coefficients was revealed by comparing propyl-, cyanopropyl-, and phenyl-functionalized films. The strongly polar phenyl groups decreased the mean diffusion

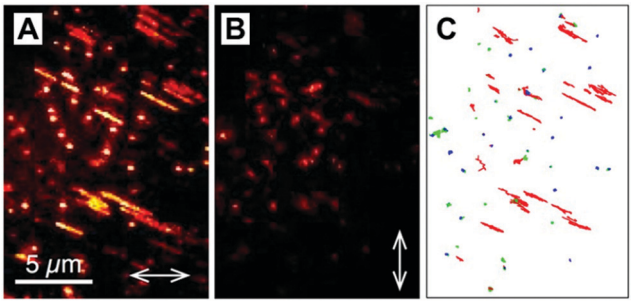

Fig. 8 SMF imaging of one-dimensional diffusion of TDI dye molecules in surfactant templated mesoporous silica. (A and B) *Z*-Projection images depicting Nile Red motions in a surfactant-templated mesoporous silica film under orthogonal emission polarization detection (white double-ended arrows). (C) Single molecule trajectories obtained by tracking the molecules where different colors indicate immobile (blue), 1D diffusing (red), and 2D diffusing (green) molecules. Figures are adapted from ref. 21 with permission. Copyright 2016 American Chemical Society.

coefficient of the dye molecule, while it was the opposite in the nonpolar propyl- and cyanopropyl-functionalized films. This study provided direct experimental evidence that molecular diffusion can be controlled by varying the density and chemical nature of the functional groups within the confined space.

Higgins *et al.* employed spectroscopic and polarization-dependent SMT to determine the mass transport of the polarity-sensitive dye Nile Red (NR) confined in surfactant-filled mesoporous silica films incorporating hexagonally ordered cylindrical pores (Fig. 8).[21] They observed that NR confined in the cylindrical pores exhibited 1D diffusion with $\sim\times 10^3$-fold smaller diffusion coefficients than in bulk solution. The hydrophobic NR molecules were found to be mostly located in the hydrophobic core regions of the micelles (having polarities similar to that of *n*-hexane), instead of being near the silica/surfactant interface. Furthermore, single molecule emission polarization (SMEP) measurements demonstrated that the NR molecules were orientationally confined to $\sim$0.6 nm diameter pathways within the pores, which was much smaller than the physical diameter of the pores.

3. Chemical reactions under nanoconfinement

Synthetically generated confinement systems could enhance the performance of encapsulated active centers, such as acid, base, and metal sites. The altered chemical and physical behaviors of substrate molecules within nanometer-sized pore structures are often attributed to the nanoconfinement effects. For example, the confining materials can directly alter the chemical reaction mechanism by assisting the chemical bond formation/breaking in zeolites and carbon nanotubes.[58–61] Chemical reaction rate and product selectivity are often dependent on the morphological properties of the confining environment in both enzymes and synthesized porous materials.[62–64] Furthermore, interfacial interactions (*i.e.*, electrostatic, van der Waals force, *etc.*) between substrate molecules and the pore surface of confining materials can also dramatically change mass transport[14,65,66] and adsorption–desorption equilibrium,[5,67] thus either enhancing or reducing catalytic reaction activities and selectivities significantly.

Porous catalysts are complex systems with different structural features and physicochemical properties, resulting in distinct local nanoconfinement environments. Such heterogeneities exist among individual catalyst particles as well as within a single catalyst at the sub-particle level. Nanoconfinement effects on chemical reactions in porous catalysts have been studied both theoretically with simplified model systems[68–71] and experimentally at the ensemble level.[10,72–75] On one hand, theoretical modeling and studies, without any doubt, are important and useful for understanding the nanoconfinement effects. However, it is limited due to the gap between the simplified model systems used in theoretical studies and the much more complex systems employed under realistic conditions. On the other hand, the ensemble measurement of catalytic reactions in porous catalysts can investigate the nanoconfinement effects under operando conditions, but it lacks the sensitivity down to the single molecule level. To improve the efficiency of porous catalysts through a rational design of nanoconfinement, it is imperative to know the quantitative correlation between the properties of nanoconfinement and the heterogeneous catalytic dynamics of confined active centers. Single molecule localization microscopy (SMLM) imaging of heterogeneous catalysis in porous catalysts is one way to search for the answer. In this section, we will cover the principle of SMLM and its applications in the study of nanoconfinement effects on heterogeneous catalysis in various porous materials.

3.1. Single molecule localization microscopy imaging of catalytic reactions

Single molecule localization microscopy (SMLM) relies on having sparsely distributed fluorescent molecules that can be isolated both temporally and spatially.[76] The positions of these individual molecules with nanometer precision can be used to reconstruct images with $<$10 nm lateral resolution and $<$20 nm axial resolution.[77] The switching between a fluorescent state (on state) and a nonfluorescent state (off state) for photoactivatable fluorophores is one of the working principles since it allows single molecule detection in condensed labeling conditions in samples. The on–off switching dynamics of dye molecules had also been achieved through a technique named points accumulation for imaging in nanoscale topography (PAINT),[78] where the reversible binding/unbinding of dye molecules to the substrate was utilized to achieve single molecule isolation. Similarly, a fluorogenic chemical reaction, wherein a nonfluorescent reactant molecule is chemically converted to a highly fluorescent product molecule (Fig. 9A), can also lead to on–off dynamics (Fig. 9B and C).

The on–off dynamics of fluorogenic reactions on the catalysts can be monitored in real time with an optimized experimental setup. Technical considerations include minimizing the fluorescence background with a total internal reflection fluorescence microscope (TIRFM), enhancing detection sensitivity with single-photon counting EMCCD cameras, using highly purified and

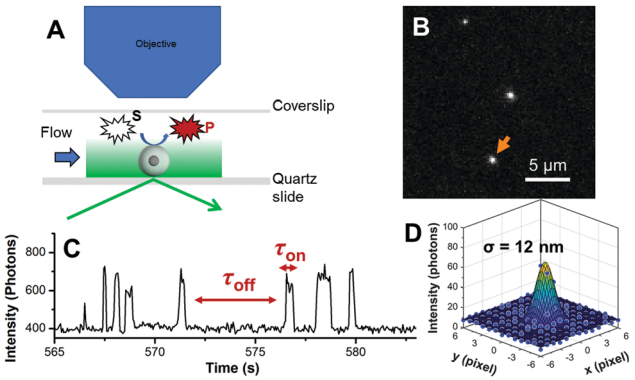

Fig. 9 Single molecule localization microscopy imaging of catalytic reactions. (A) SMF imaging of the oxidation of amplex red catalyzed by platinum loaded core–shell mesoporous silica particles under TIRFM. (B) Typical fluorescence image of freshly generated fluorescent product molecules. (C) Segment of fluorescence intensity trajectory on a single nanocatalyst highlighted in (B). τ_{off} and τ_{on} are determined at turn-over resolution. (D) Gaussian fitting of the intensity distribution of the highlighted single molecule image gives the molecular center position with a 12 nm localization precision. Figures are adapted from ref. 118 with permission. Copyright 2020 American Chemical Society.

clean reagents, and removing desorbed fluorescent product molecules using a flow system. The positions of freshly generated fluorescent product molecules can be determined with nanometer precision (Fig. 9D) to pinpoint the locations of catalytic active sites on a single catalyst. Transmission electron microscopy (TEM) and scanning electron microscopy (SEM) images are often taken to correlate the different structures on single catalyst particles with their catalytic activities from single molecule studies.[79] A recently published review article discussed the importance of correlating SFM imaging results with SEM images to establish the structure–activity relationship in heterogeneous catalysis, especially for catalysts containing complex structures.[80] Beyond the benefits of the high spatial resolution in SMLM for resolving locations of catalytic active sites, the single molecule on–off dynamics enables a quantitative measurement of temporary properties, including reactant reaction kinetics, product dissociation kinetics, and catalyst stability at turn-over resolution.

Fluorogenic probes for single molecule fluorescence imaging. The success of single molecule fluorescence imaging of chemical reactions on catalyst surfaces relies on choosing an appropriate fluorogenic probe. First, the catalytic center should be active for the chosen fluorogenic reaction. Second, there should be a sufficient contrast of fluorescence emission brightness between reactant and product molecules. Ideally, the reactant should make no contribution to the fluorescence background. Third, the overlap between the fluorescence signals of the product molecules and the fluorescence background from the catalyst should be very small (or ideally avoided entirely). So far, many fluorogenic reactions that can be used for SMF imaging have been reported. For example, nonfluorescent fluorescein dye-based derivatives including APF, HPF,[81] H_2DCFDA, carboxyl-H_2DCFDA, chloromethyl-H_2DCFDA, and deacetylated H_2DCFDA[82] can generate highly fluorescent product molecules upon oxidation; DN-BODIPY,[83] resazurin,[84] and DCDHF-azide and its derivatives[85,86] can generate highly fluorescent product molecules by reduction; CalFluors[87–89] can also be converted to highly fluorescent molecules upon a copper-catalyzed click reaction with alkyne.[90] Furthermore, coupling reactions (such as Suzuki, Heck, or Stille reactions) catalyzed by noble metal NPs (such as Pd, Pt, and Rh) to add aryl, vinyl, or alkyl groups can also turn on the fluorescence.[91–94] A more detailed summary is given in Fig. 10. Some of these fluorogenic probes (*e.g.*, amplex red, resazurin, APF, CalFluors, *etc.*) are readily available from commercial sources, while the synthesis protocols for other fluorogenic probes have been fully described in previous publications.

Super-resolved mapping of catalytic active sites. SMLM has been used to recover heterogeneities in catalysis at different structures such as facets, edges, and defects in single solid catalysts, such as metals, semiconductor particles,[95–97] crystals,[98,99] and nanowires.[100,101] Quantitative correlations between the structural properties of catalysts and the catalytic activity have been unveiled. Weckhuysen *et al.* used SMF imaging together with super-resolution optical fluctuation imaging (SOFI) analysis to investigate the inhomogeneity in the distributions of zeolite aggregates at the sub-micrometer level as well as in acidic catalytic activities among different zeolite aggregates embedded inside real-life FCC particles with sizes of 50–150 μm.[102]

Typically, quantitative correlations between structural features and the catalytic activity are explored to reveal the structure–property relationship, which can be provide guidance for the rational design of high-performance catalysts. SMF imaging studies of these catalysts are carried out in real time and under realistic conditions, unlike other methods such as TEM and STEM which allow the characterization at higher spatial resolution, but lack dynamic information and usually require vacuum or low-pressure conditions. Vibrational spectroscopy can measure the adsorbed reactants and products on surfaces under realistic conditions, but lacks single-molecule sensitivity without an extraordinary enhancement. Often, a combination of results from all the aforementioned techniques is necessary to fully recover and understand the surface reactions on a single catalyst.

Deconvolute catalytic dynamics at the nanoscale. Kinetic processes in a chemical reaction catalyzed on the catalyst surface involve the adsorption, diffusion, activation, and chemical conversion of the reactant, and the desorption of the final product. The elementary processes that are related to the rate-limiting step(s) will determine the turnover frequency of a catalytic reaction. The physicochemical properties (*e.g.*, structure, chemical composition, and electronic properties) of the active sites in a single catalyst particle as well as between different catalyst particles are often heterogeneous, resulting in inhomogeneities at each kinetic step and the overall catalytic reaction performance. The capability of deconvoluting these kinetic processes in a catalytic reaction and correlate them to specific structural and physicochemical properties of a catalyst is essential to establish the structure–property relationship and guide the rational design of highly efficient catalysts. SMF imaging offers such a crucial capability.

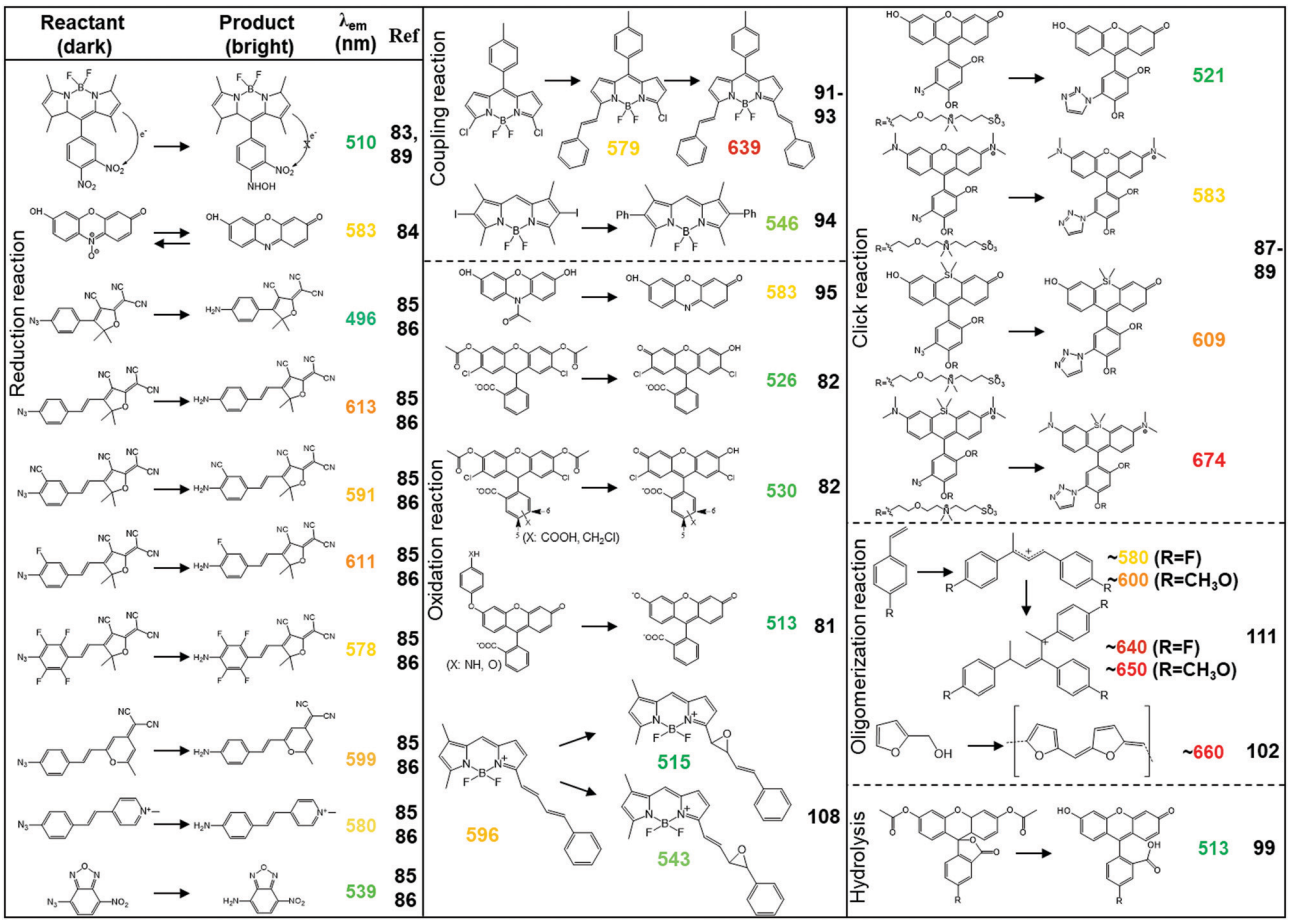

Fig. 10 Fluorogenic probes for single molecule imaging of chemical reactions.

In SMF imaging of a fluorogenic reaction on a catalyst, one can obtain a typical fluorescence intensity curve over time as shown in Fig. 9C with two distinguishable waiting periods: τ_{off} for the product formation and τ_{on} for the product dissociation from the catalyst surface. Statistical analysis of these τ_{off} and τ_{on} values collected over a sufficient imaging time, by using either the arithmetic average or exponential decay fitting their distributions, gives the average waiting times $\langle\tau_{off}\rangle$ and $\langle\tau_{on}\rangle$. The inverse values, *i.e.*, $\langle\tau_{off}\rangle^{-1}$ and $\langle\tau_{on}\rangle^{-1}$, are used as the product formation rate and dissociation rate, respectively. The kinetic data of both product formation and dissociation can then be obtained by repeating such quantitative measurements with different reactant concentrations. Fitting the obtained kinetic data could resolve kinetic parameters, including the adsorption/desorption equilibrium constant ($K_1 = k_1/k_{-1}$) and the reaction rate constant (k_{eff}), in the individual dynamic processes in a catalytic reaction (Fig. 11).

For heterogeneous catalysis on the catalyst surface, by fitting the reaction kinetic data using the classic Langmuir–Hinshelwood surface reaction model, the kinetic parameters K_1 and k_{eff} can be determined.[103]

$$\upsilon_r = \langle\tau_{off}\rangle^{-1} = \frac{k_{eff}K_1[S]}{1 + K_1[S]} \quad (7)$$

On the other hand, two possible parallel product dissociation pathways: a direct dissociation pathway (step iv) and a reactant-assisted pathway involving the participation of the reactant (step ii and iii) can exist in the waiting time τ_{on}. By fitting the dissociation kinetic data with the Langmuir–Hinshelwood model, the kinetic parameters k_2, k_4, and K_2 can be determined, where $K_2 = k_3/(k_{-3} + k_4)$.[103]

$$\upsilon_d = \langle\tau_{on}\rangle^{-1} = \frac{k_4K_2[S] + k_2}{1 + K_2[S]} \quad (8)$$

Since this approach for the quantitative analysis of kinetics in a catalytic reaction can be performed at the single-catalyst particle and single molecule level with turn-over temporal resolution, it enabled one to discover inhomogeneous behaviors in both catalytic activities and dissociation mechanisms among catalysts of the same type. Moreover, such quantitative analysis of dynamic processes can also be done in sub-regions on a single catalyst particle when the spatial resolution in SMLM is sufficiently higher than the physical size of the particle. In SMLM imaging, the temporal information when the fluorescent molecule is detected is also stored accordingly with the molecular position. The super-resolved mapping enables one to differentiate subregions on a single catalyst particle and extract molecular spatial and temporal information in the corresponding regions.

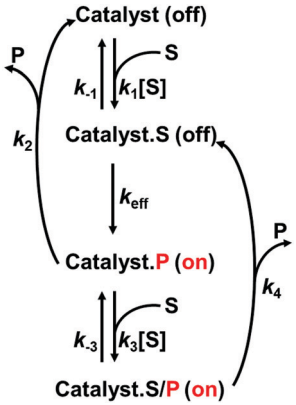

Fig. 11 Reaction dynamics on catalysts. S: reactant/substrate, P: product.

Thus catalytic dynamics in isolated subregions can be quantitatively measured.[98]

Unveil the temporal dynamics of catalytic reactions at the nanoscale. Like enzymes,[104] the activities of solid catalysts vary temporarily. Many factors can contribute to temporal fluctuations of reaction activity on a catalyst, such as dynamic surface restructuring during chemical reactions. Inhomogeneity in fluctuation rates often exists at different surface structures, sites, as well as among individual catalysts. Such temporal dynamics and inhomogeneities are not accessible in ensemble-averaged measurements. In SMLM imaging, one can readily acquire temporal dynamics of chemical reactions by statistically analyzing the on–off times in the turn-over reaction (Fig. 9C).

Weckhuysen *et al.* investigated the reversible proton transfer processes between two aromatic molecules (*i.e.*, 4-methoxystyrene and 4-fluorostyrene) and Brønsted acid sites in porous materials, zeolite ZSM-5 (Fig. 12).[105] The on–off fluorescence of probe molecules is caused by the conversion between its carbocationic (on) and neutral formats (off) through the proton-transfer reaction at Brønsted acid sites. The fluorescence intensity blinked differently between the two probe molecules and among individual molecules. The subsequent pairs of off-state (τ_{off}) and on-state (τ_{on}) over many individual molecules for the two probe molecules were statistically analyzed to reveal the distribution of long- and short-lived fluorescence events as well as their correlation in the time domain. The highly heterogeneous distributions suggest that the stability of fluorescent carbocationic species largely depends on their local environments. The on–off dynamics, *i.e.*, the proton-transfer reaction rates, could be affected by changing the solvent environment, such as introducing *n*-heptane would cause faster protonation rates for 4-methoxystyrene; however, when using 1-butanol, an opposite effect would occur.

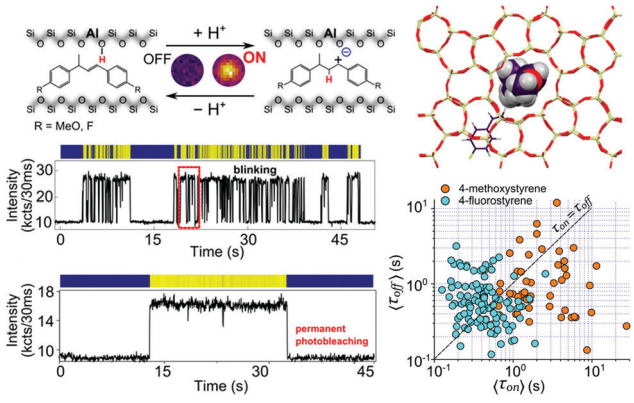

Fig. 12 Single molecule fluorescence imaging of the reversible proton-transfer reaction and the stability of fluorogenic probes formed through styrene oligomerization in zeolites. Figures are adapted from ref. 105 with permission. Copyright 2018 American Chemical Society.

Chen *et al.* studied the time dependence of the turnover rates on single gold nanoparticles by calculating the autocorrelation function ($C_\tau(m)$).[103,104] The decay times obtained by fitting with the exponential decay functions were used to determine the fluctuation rates of both product formation and dissociation processes. The unveiled fluctuation dynamics was attributed to small-scale surface restructuring at specific reactive sites. The results showed that the surface reconstruction rates were positively correlated to the catalytic turnover rates. A large difference in temporal fluctuation dynamics was observed between the two chemical processes (τ_{off} and τ_{on}), which indicated that the docking sites wherein the product molecules dissociate could be different from the catalytic sites.

3.2 Effects of intraparticle mass transport

It is well known that heterogeneous catalysis is an interplay between mass transport and chemical reaction. Generally, the chemical conversion is considered as the rate-limiting step in catalysis on catalyst surfaces such as the aforementioned LDH, titanium dioxide crystal, and metal nanoparticles. The mass transport of the reactant is usually much faster than the chemical reaction. However, the mass transport of the reactant cannot be ignored when catalytic reactions occur within the confined space in all types of porous materials (*e.g.*, zeolites, metal–organic frameworks, carbon nanotubes, mesoporous particles, *etc.*). The accessibility of reactant molecules to the catalytic active sites confined in these porous materials are essential for optimal use of the materials. Undoubtedly, understanding the role of intraparticle mass transport in catalysts is even more important for industrial applications such as using ZSM-5 in the petroleum industry. The following are some examples of using SMF imaging to unveil the role of molecular mass transport during the catalysis in porous materials.

Mobil Composition of Matter (MCM). MCM is a type of mesoporous material composed of a hierarchical structure from a family of silicate and aluminosilicate solids, which are often used as catalysts or catalyst supports. MCM-41 materials are composed of a hexagonal array of pores with a uniform diameter that can be tuned between 1.5 and 10 nm. Ensemble measurements have shown that smaller Ti-MCM-41 particles have better catalytic selectivity and higher activity than bigger ones for the epoxidation of cyclohexene and cholesterol.[106,107] It was believed that the intraparticle diffusion limits the full usage of Ti sites in the porous materials. Therefore, reducing the particle size will promote the optimal use of confined Ti sites in the MCM-41 particles.

Roeffaers *et al.* studied the effects of intraparticle diffusion on the catalysis of titanium sites confined in porous MCM-41 at the single-particle single molecule level (Fig. 13).[108] The epoxidation of phenylbutadienyl-substituted boron dipyrromethene difluoride (PBD-BODIPY) probe molecules was used as a model reaction wherein a blue shift of fluorescence will be generated. Super-resolution mapping of the locations of active Ti sites in MCM-41 particles unveils that only an ~300 nm region in the outer part of the particles is responsible for the catalytic reaction, thus contributing to the overall activity. Together with control experiments and material characterization of particles, the SMF imaging results reveal the fact that only in a submicrometer fraction of particles would the Ti sites be fully utilized for catalysis because of the limitation of intraparticle molecular transport.

Zeolites. Hofkens *et al.* investigated the catalytic reaction of furfuryl alcohol at acidic sites in Zeolite Socony Mobil-5 (ZSM-5) to generate a highly fluorescent product.[109] ZSM-5 is widely used in the petroleum industry as a heterogeneous catalyst for hydrocarbon isomerization reactions. ZSM-5 has porous structures with medium pore sizes of ~0.5 nm. It contains two intersecting three-dimensional channels, including straight parallel pores and sinusoidal pores of a 10-membered ring. Probed by the combination of focused-ion-beam (FIB), transmission electron microscopy, and electron diffraction pattern analysis, two zones with different crystallographic orientations of 90° intergrowth had been observed (Fig. 14A). Using SMF imaging, they reconstructed a super-resolution mapping of activities in the ZSM-5 crystal. A 20–60 nm wide highly active region at the boundary of the 90° intergrowth was revealed (Fig. 14B). The enhanced catalytic activity in this zone can be explained by the fact that locally there is reagent influx from two crystal faces *via* both the sinusoidal and the straight pores, rather than the difference in the activity of local acidic sites. These heterogeneous catalytic activities at the nanoscale are hidden in traditional ensemble measurements. They also used single molecule fluorescence imaging to investigate the effects of steaming of H-ZSM-5 crystals on the catalysis efficiency (Fig. 14C).[110] They found out that mild steaming of H-ZSM-5 crystals at 500 °C (H-ZSM-5-MT) notably increases the catalytic activity by enhancing the accessibility of acidic sites by altering the porosity *via* dealumination. The steaming also causes a highly heterogeneous distribution of accessible acid sites at the macroscopic level. However, a significant loss of acidic sites and a much lower catalytic activity were observed when steaming at a higher temperature (700 °C, H-ZSM-5-ST). Later, they also discovered that the catalytic activity of the oligomerization of styrene derivatives by H-ZSM-5 crystals largely depends on the local polarity and structure (pore types and sizes) of the confined space, as well as the chemical properties (moiety) of the reactant molecules using SMF microscopy imaging (Fig. 14D).[111]

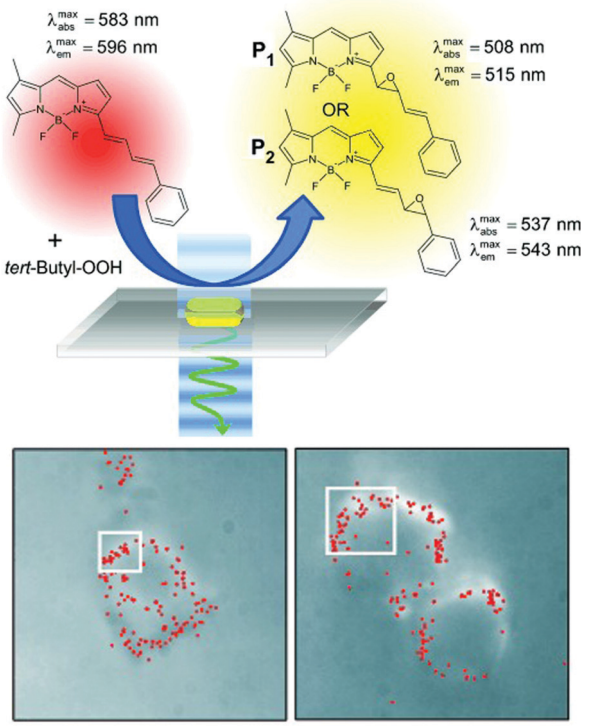

Fig. 13 Single-particle single molecule imaging of the epoxidation of PBD-BODIPY in Ti-MCM-41 particles. Schematic view of the epoxidation of PBD-BODIPY in Ti-MCM-41 particles and two examples of individual turnover measurements on Ti-MCM-41 particles. Figures are adapted from ref. 108 with permission. Copyright 2010 Wiley-VCH.

In another example, Roeffaers *et al.* studied the effects of a hierarchical porous structure on the catalytic activity of dealuminated mordenite zeolites using SMF microscopy imaging.[112] The acid-catalyzed condensation reaction of furfuryl alcohol was used as the model reaction. It had been believed that intracrystalline diffusion limitations could be overcome by introducing larger extraframework meso- and macro-porosity into the solid catalyst, which enhances the effectiveness of porous catalysts. However, the effects of the introduced extraframework pore structures on local nanoscale catalytic activities were not clear. The SMF imaging experiments show that catalytic turnovers mostly happen within aligned micropores, while the reaction activity in extraframework pores is much lower. Although the intraparticle diffusion can be overcome by the introduction of extraframework pores, it also causes the loss of original active sites at the location of the extraframework pores, thus reducing the optimal use of all catalytic sites inside the porous particles.

Ruthenium catalyst complex. Blum *et al.* studied the polymerization reactions in a porous ruthenium (Ru) catalyst complex composed of numerous individual living polymer strands associated with ruthenium catalyst and untagged norbornene (Fig. 15).[113] The catalytic active centers of Ru catalysts were embedded inside the porous complex. Two types of Ru-catalyzed polymerization reactions were investigated, including the chain elongation reaction and the chain terminalization reaction. These two polymerization reactions were imaged at the single molecule level with turn-over resolution simultaneously using two different reagent molecules tagged with fluorescent probes of different fluorescent emission spectra. The super-resolved spatial and temporal results of the two catalyzed polymerization reactions showed different dynamic responses, reflecting the different

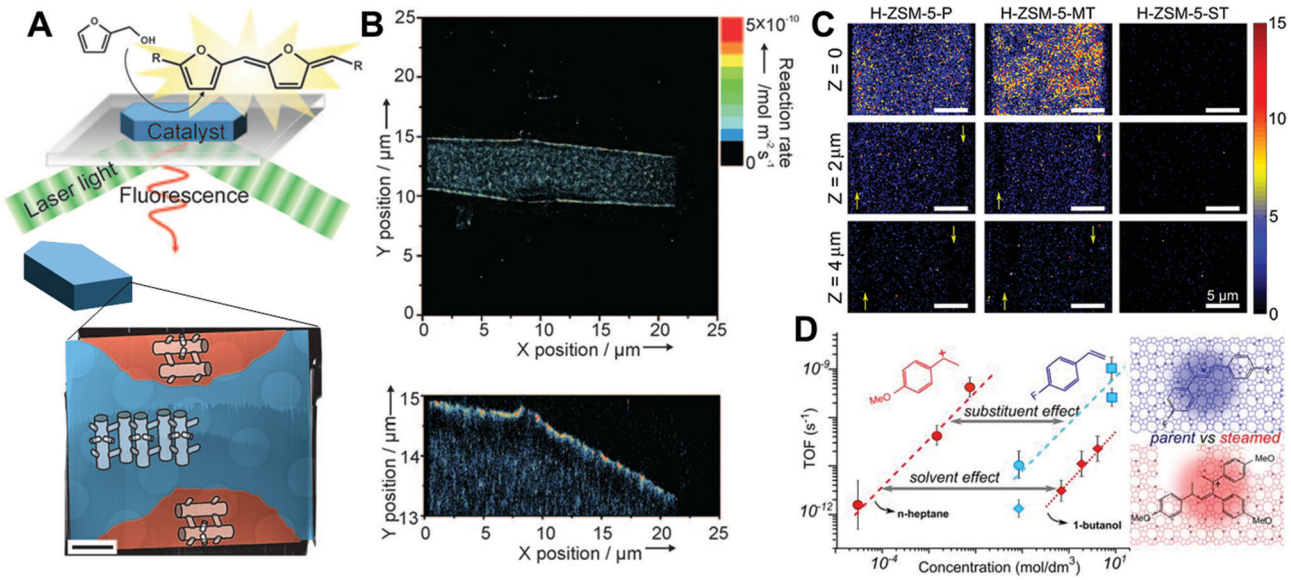

Fig. 14 SMF imaging of heterogeneous catalysis in ZSM-5 zeolites. (A) Schematic view of the acid catalyzed reaction of furfural alcohol polymerization (top) and crystal orientation indicated by color and a schematic representation of the channel system from FIB-TEM characterization. (B) Super-resolution mapping of acidic sites and activities in ZSM-5. Figures (A and B) are adapted from ref. 109 with permission. Copyright 2009 Wiley-VCH. (C) 3D super-resolution mapping of acidic sites and activities in ZSM-5 after steaming treatment where H-ZSM-5-P, H-ZSM-5-MT, and H-ZSM-5-ST represent parent, 500 °C, and 700 °C treated ZSM-5, respectively. The color bar indicates turnover rates per 200 × 200 nm^2. Figures are adapted from ref. 110 with permission. Copyright 2015 American Chemical Society. (D) Effects of pore physicochemical properties on the acid-catalyzed reaction in ZSM-5. Figures are adapted from ref. 111 with permission. Copyright 2016 American Chemical Society.

effects of the local catalyst microenvironments on reaction dynamics. Considering the continuously catalyzed polymerization reactions surrounding the Ru active center would increase the local polymer density, induce conformational changes, and reduce the accessibility of reagents. Therefore, possible explanations for the different spatial–temporal variations of catalytic activities of the investigated chain elongation and termination reactions are attributed to diffusion differences between the two reagents since their chemical structures and molecular sizes are very different.

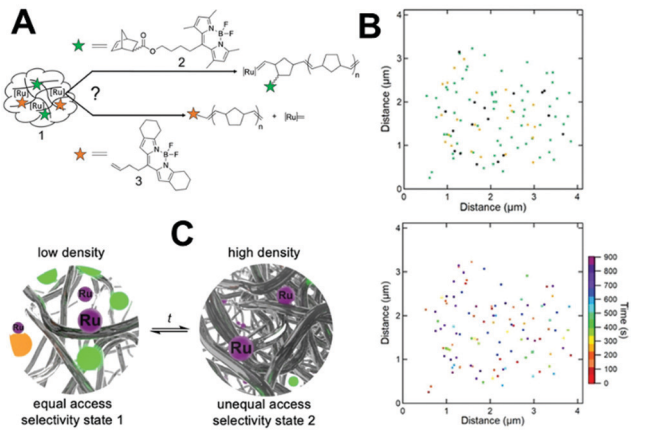

Fig. 15 SMF imaging of the polymerization reaction in the Ru-complex. (A) Schematic of two different polymerization reaction pathways: single chain-elongation and -termination. (B) Super-resolution mapping image of single chain-elongation (green) and -termination (orange) events observed at a single polymer-particle aggregate, with events not identified with statistical confidence (top), and of all single-turnover events, where the color of data points indicates the reaction time. (C) Hypothesized physical model for selectivity changes. Figures are adapted from ref. 113 with permission. Copyright 2020 Wiley-VCH.

3.3 Reaction dynamics of heterogeneous catalysis under nanoconfinement

To further understand the nanoconfinement effects on the dynamics of heterogeneous catalysis on active centers in porous materials, a well-defined catalyst system is needed. Ideally, a single reaction center in a well-defined and highly tunable nanoconfinement structure should be created for single molecule catalysis investigation. In this configuration, the effects of the properties of nanoconfinement including structural features, physicochemical properties, and electrostatic forces on chemical reaction dynamics including mass transport, adsorption/desorption, chemical conversion of reactants and diffusion and desorption of products can be systematically investigated at the single molecule level.

Platinum nanoparticles in mesoporous silica. Although lots of single molecule imaging porous materials (*e.g.*, thin films, porous particles) have been investigated to understand the physicochemical properties of the pore environment on mass transport, simultaneous measurements of the mass transport and reaction dynamics in nanopores inside the complicated porous materials have been very challenging. To overcome this obstacle, we took advantage of a well-defined core–shell catalyst platform where the catalytic centers (metal nanoparticles) are confined at the end of nanopores with controlled lengths in a mesoporous silica dioxide ($mSiO_2$) shell (Fig. 16).[114] We studied

the dynamic behavior of catalytic processes under nanoconfinement including mass transport and catalytic reactions at the single molecule and single particle level *in situ*.

Confining catalytic active centers in mesoporous silica has been a very useful strategy for designing high-performance catalysts. Many benefits can be obtained through the confined structure. For example, encapsulating nanoparticles in mesoporous silica materials can stabilize the particle morphology and avoid the aggregation of particles during the removal of surfactant ligands. Moreover, mesoporous silica is essentially the same material like glass, making it transparent to create a clean background for fluorescence imaging. Furthermore, this catalyst structure provides a restricted pathway for reactant molecules in the bulk solution to diffuse a uniform distance, defined by the thickness of the $mSiO_2$ shell, to access the active sites on confined platinum NPs placed at the bottom of the nanopores. In this well-defined catalyst platform, it has two obvious benefits. First, one can confidently track the one-dimensional mass transport of fluorescent molecules in the linear nanopores. Local environments, including pore structures and viscosities, can be quantitatively evaluated. Second, the single molecular trajectory analysis provides an accurate measurement of molecular diffusion in nanopores under reaction conditions, which then enables further analysis to decouple the influence of molecular transport and reaction kinetics. A quantitative measurement of molecular diffusion in nanopores using single molecule tracking experiments shows $\sim 10^4$ times slower mass transport in nanopores than in bulk conditions.

In this specific study, the platinum nanoparticle (Pt NP) catalyzed oxidation reaction of amplex red was used as the model reaction to evaluate nanoconfinement effects. Under 0.02 μM of amplex red, the amount of amplex red molecules that approach the Pt NPs in an ~ 2 nm nanopore was estimated to be 4×10^{-26} mol s^{-1}, while the experimentally measured single-particle catalytic activity is 3×10^{-26} mol s^{-1}. Therefore, the catalytic reaction rates are limited by the mass transport at low concentrations of amplex red. However, the effect of mass transport on catalytic reaction rates is not significant at higher concentrations. A modified kinetic model taking into account the mass transport factor was established to accurately fit the kinetic data and determine kinetic parameters (*e.g.*, adsorption/desorption equilibrium constant K_{AR} and reaction rate constant k_{eff}) under nanoconfinement. On the contrary, the mass transport of the reactant is negligible when no mesoporous shell is present around Pt NPs. The kinetic data can then be directly fitted by the Langmuir–Hinshelwood surface reaction model to determine K_{AR} and k_{eff}. From the single particle single molecule kinetic data, the measured k_{eff} is around seven times higher and K_{AR} is around two times smaller for Pt NPs under nanoconfinement. Possible reasons, including effective concentrations and physical constraints of the adsorbed substrate molecules, are used to explain the observed catalytic reaction dynamics under nanoconfinement.

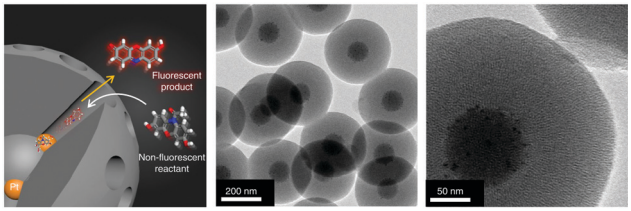

Fig. 16 Multi-layer core–shell porous particle as a model platform for simultaneously studying mass transport and heterogeneous surface catalysis. Figures are adapted from ref. 114 with permission. Copyright 2018 Nature Publishing Group.

Gold nanoparticles in carbon nanotubes. Carbon nanotubes (CNTs) have been widely used as supporting materials for metal particle catalysts because of their well-defined hollow interiors, high surface area, remarkable mechanical properties, and thermal stability. Metal particles as catalytic active centers have distinct activities when loaded inside the hollow structure of CNTs compared to those supported on the external surface of CNTs.[72] When metal particles are loaded inside CNTs, the nanoconfinement effect occurs.

To understand the difference in the catalytic properties of gold nanoparticles at the two types of loading sites, Kang *et al.* synthesized Au nanoparticles deposited on the outer surface (Au/CNTs-out) and inner surface (Au/CNTs-in) of CNTs and monitored the reduction reaction of resazurin using single molecule fluorescence imaging (Fig. 17).[115] Both reaction kinetics of the reactant resazurin ($\langle\tau_{off}\rangle^{-1}$) and dissociation kinetics of the product resorufin ($\langle\tau_{on}\rangle^{-1}$) for four types of catalyst, *i.e.*, Au/CNTs-out, Au/CNTs-in, Au nanoparticles, and CNTs, were quantitatively determined at the single molecule level with turn-over resolution. Fitting the reaction kinetics gives the highest catalytic activity (k_{eff}) for Au/CNTs-out. Au/CNTs-out also shows the largest adsorption strength (K_1) of resazurin. For product dissociation, the same dissociation mechanisms are observed for all four catalysts. The reactant assisted dissociation pathway (k_2) is faster than the direction dissociation pathway (k_3). Both k_2 and k_3 are larger for Au/CNTs-out, suggesting a weaker binding strength of the product resorufin than that for Au/CNTs-in. By comparing to unsupported gold nanoparticles, the experimental results show that the gold nanoparticles confined inside CNTs show a lower catalytic activity, a weaker adsorption strength of the reactant molecule, and a stronger binding strength of the product molecule. On the other hand, the opposite trend was observed for gold nanoparticles supported on the external surface of CNTs. Kang *et al.* attributed this opposite trend to the higher density of electrons on the external surface of CNTs as electrons would shift from the inner to the outer surface of CNTs due to their curved walls. The more electron-rich environment for gold nanoparticles on the external surface of CNTs would facilitate the reduction reaction of resazurin.

3.4 Effects of pore morphology

Using the well-defined core–shell nanocatalyst platform (Fig. 16), we studied the nanoconfinement effects on the catalytic reaction dynamics under variable nanopore morphologies, including pore length and diameters at the single-molecule and single-particle level.[116] The nanoconfinement effects on catalytic reaction kinetics

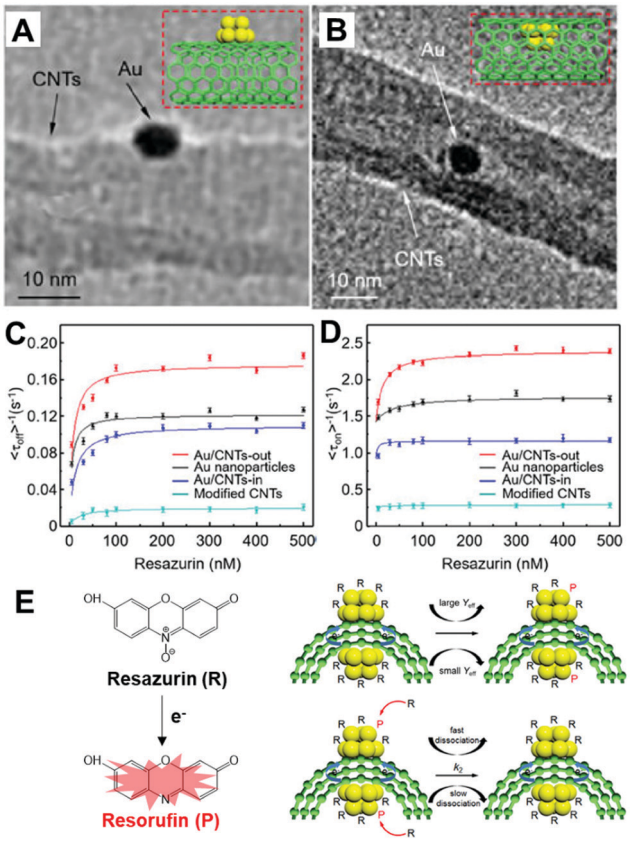

Fig. 17 SMF imaging of the support-effects of gold nanoparticles on carbon nanotubes. TEM images showing gold nanoparticles outside (A, Au/CNTs-out) and inside (B, Au/CNTs-in) carbon nanotubes. Catalytic reduction reaction kinetics of resazurin (C) and dissociation kinetics of resorufin (D) in four nanocatalysts. (E) Proposed kinetic mechanisms of the product formation and dissociation processes on Au/CNTs-out and Au/CNTs-in. Figures are adapted from ref. 115 with permission. Copyright 2018 Wiley-VCH.

(*i.e.*, molecular adsorption strength and reaction rate) were discovered to be dependent on nanopore morphology. Intuitively, one would expect a decreasing activity when the catalytic center (Pt) is blocked from the reactant molecules by obstacle objects such as the mesoporous silica shell in this work. Moreover, one would also expect the catalytic activity reduction because the blocking effects from the $mSiO_2$ shell would be stronger when the shell gets thicker and the nanopore gets narrower. However, we observed that the catalytic reaction activity (k_{eff}) increases, rather than decrease, when the shell becomes thicker (0–120 nm) and the nanopore diameter changes from ~3 to 2 nm (Fig. 18). The ensemble measurements of catalytic activities of the same core–shell particles also show the same results. On the other hand, the nanoconfinement on molecular adsorption strength (K_{AR}) is only sensitive to nanopore diameter where a weaker adsorption strength is present inside nanopores of a smaller diameter due to the less motion freedom in the narrower pore. Furthermore, experimental results also show that the activation energy (E_a) for the oxidation of amplex red catalyzed by Pt NPs in nanopores is reduced but is independent of pore length. The reduced activation energy agrees with the enhanced catalytic activity under nanoconfinement.

3.5 Effects of the chemical environment on catalytic dynamics

The surface properties of porous materials play pivotal roles for their applications in separation, drug delivery, and catalysis. In catalysis science, modifying porous silica materials by grafting the silica surface with acid, base, or other organic functional groups could induce new or enhanced reactivity in chemical reactions. For example, organosulfonic acid-functionalized mesoporous silica materials have been used in the esterification of fatty acid for biodiesel production.[117] For chemical reactions that involve hydrophobic reactants and/or hydrophilic products, modifying the pore surface with hydrophobic functional groups could enrich reactants within the pores and repel products from the pores, and thus enhance the reaction rate.

Using SMF imaging, we revealed the effects of environmental hydrophobicity on molecular dynamics during the Pt-catalyzed oxidation of hydrophobic amplex red in ~3 nm silica nanopores (Fig. 19).[118] The silica nanopore surface was functionalized with $-SO_3H$ or $-CF_3$, creating hydrophilic or hydrophobic environments, respectively. A higher catalytic activity, a stronger adsorption strength, and a higher activation energy were unveiled in hydrophobic nanopores as compared to those in hydrophilic nanopores. The seemingly counterintuitive results between a higher catalytic activity and a higher activation energy in nanopores are due to the confinement effects on trapping intermediate species. The local enrichment of the intermediate amplex red (AR) radicals in the hydrophobic nanopores is more significant than that in the hydrophilic nanopores, which is supported by evidence from both single molecule tracking and incubation of resorufin (Re) with core–shell mesoporous particles where lower mass transport rates and stronger trapping capabilities of Re in hydrophobic nanopores than those in the hydrophilic nanopores were observed. Moreover, the product resorufin molecules also have very different dissociation kinetic behaviors in the two types of nanopores (Fig. 19C). At a low concentration of AR, the direct dissociation pathway dominates. The dissociation and mass transport rates are smaller in the hydrophobic nanopores, which suggests its strong confinement effects for trapping the molecules. At a high concentration of AR, the reactant assisted dissociation mechanism becomes the dominant dissociation pathway and the interplay and competition between the reactant molecule AR and the product molecule Re are important for their dynamic behaviors. A larger dissociation rate in the hydrophobic nanopores was measured, which can be explained by the stronger confinement effects of hydrophobic nanopores and much higher concentrations of the reactant molecule AR. Furthermore, the faster dissociation rate of the product molecule Re can also speed up the catalytic reactions.

3.6 Decipher nanoconfinement effects by single molecule imaging

Restricted molecular orientation reduces adsorption strength in nanopores. The orientation of molecules will be restricted in nanopores when the molecule size and pore diameter are comparable. In combination with the well-defined nanocatalyst platform and single molecule polarization fluorescence microscopy imaging,

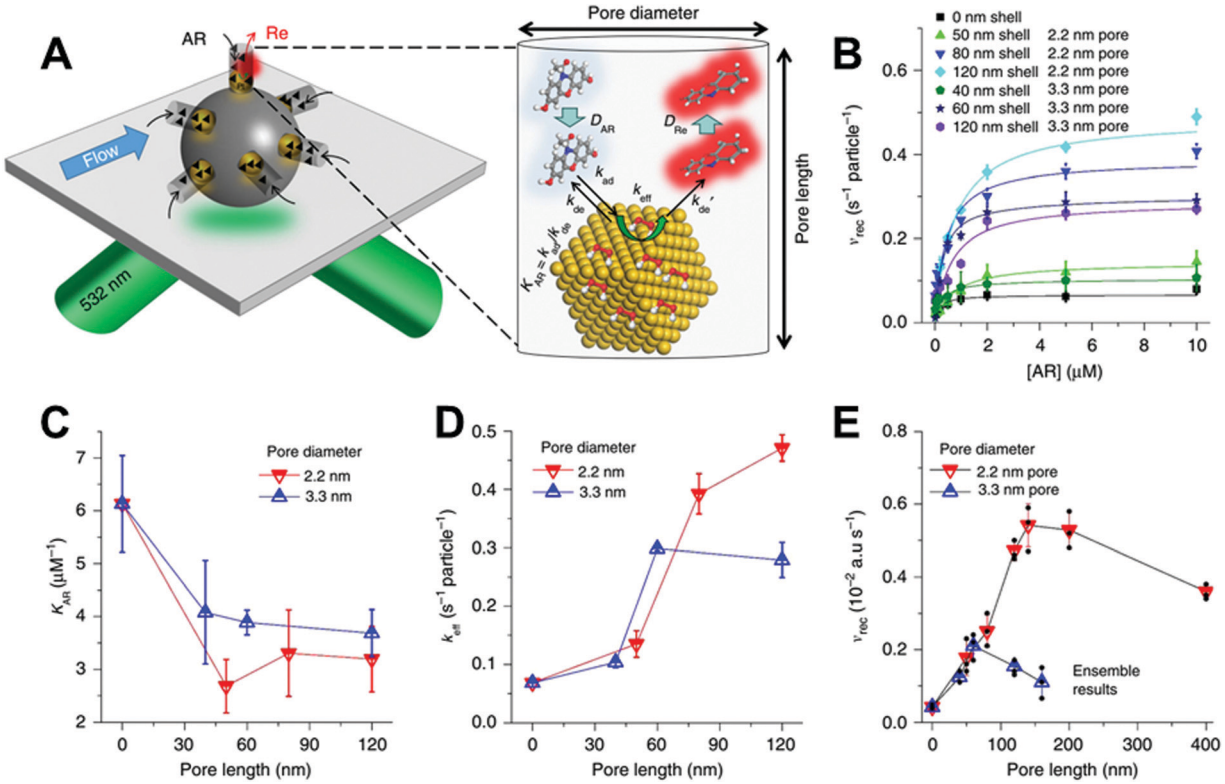

Fig. 18 Effects of nanopore morphologies on reaction kinetics in nanopores. (A) Schematic of the single-particle single molecule imaging setup (left) and chemical conversion processes inside nanopores (right). (B) Reaction kinetics for different nanopore lengths and diameters at the single-particle single molecule level. Adsorption/desorption equilibrium constant K_{AR} (C) and rate constant k_{eff} (D) are obtained by fitting the single-particle single molecule kinetic data. (E) Ensemble results of reaction rates of nanocatalysts with variable porous shell thicknesses and pore diameters. Figures are adapted from ref. 116 with permission. Copyright 2019 Nature Publishing Group.

we showed that the confined molecular orientation was the reason for the reduced adsorption strength in nanopores (Fig. 18).[116] For asymmetric aromatic molecules like amplex red and resorufin, a preferred molecular orientation wherein the long axis of the molecule aligns perpendicular to the Pt NP surface and parallel to the nanopore would be expected. Also, the resorufin molecule has absorption and emission dipole moments (μ) along the long axis of its planar structure. Using a linearly polarized excitation light source, only resorufin molecules with their absorption dipole moments parallel to the illumination light polarization direction would show strong fluorescence. Suppose that the long axis of resorufin molecules is aligned parallel to the nanopores. In that case, more resorufin molecules will be excited when the nanopores are aligned parallel to the polarization direction of the excitation light. On the contrary, if the long axis of resorufin molecules is randomly oriented in the pore, the polarized light will excite resorufin regardless of the orientation of the nanopores with the polarization direction of the excitation light. An elliptical distribution of resorufin molecules was observed with linearly polarized excitation light (Fig. 20D), while such asymmetrical distribution pattern disappeared when switching to circularly polarized excitation light (Fig. 20E). Moreover, more product molecules were detected under circularly polarized excitation light. The super-resolution imaging results here suggest the parallel alignment of resorufin molecules with nanopores. The preferential orientations of amplex red and resorufin molecules in nanopores should be the same since their molecular structures are similar. Without the confinement of the nanopores, aromatic molecules typically adsorb strongly on a precious metal surface in a laying down configuration due to the preferred interaction of the aromatic pi-orbital with the d-orbital of the metal. Therefore, the restricted molecular orientation of amplex red in nanopores would prevent the laying down adsorption configuration, resulting in a reduction in adsorption strength.

Enrichment of the reaction intermediate enhances the overall catalytic activity. The restricted molecular orientation of amplex red where the phenol group directly faces toward the surface of Pt NPs in nanopores can facilitate the catalytic reaction by increasing the probability of the phenol group reacting with reactive oxygen species (ROS), *e.g.*, chemisorbed oxygen on the Pt surface.[119] This is in agreement with and also evident by the measured lower activation energy under nanoconfinement. Nonetheless, the reduced E_a under the nanoconfinement effects still does not explain the dependence of the activity enhancement on nanopore length, *i.e.*, the catalytic activity increases when the nanopore length increases (0–120 nm, Fig. 18D). We attribute this phenomenon to the enrichment of reaction intermediate species in nanopores. For the oxidation of amplex red on Pt NPs, it involves three sequential chemical conversion steps, including forming amplex red radicals (AR$^{\bullet}$), the following

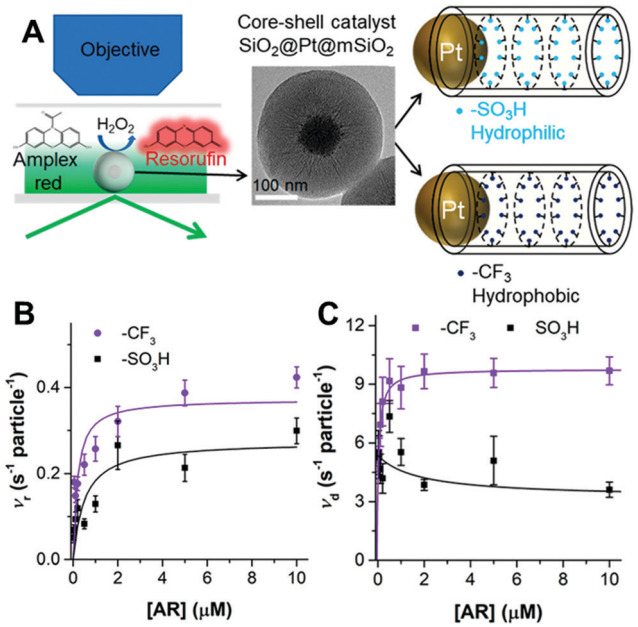

Fig. 19 Single molecule investigation of nanoconfinement hydrophobicity in heterogeneous catalysis. (A) Schematic view of the imaging experiments and high-resolution TEM images of core–shell nanocatalysts. The pore surface in the mesoporous shell was modified to be hydrophilic using $-SO_3H$ functional groups or hydrophobic using $-CF_3$ functional groups. Oxidation reaction kinetics of amplex red (B) and dissociation kinetics of resorufin (C) on Pt NPs in single core–shell nanocatalysts. Figures are adapted from ref. 118 with permission. Copyright 2020 American Chemical Society.

disproportionation reaction of two AR• to produce one AR molecule and AR^+ cation, and finally the hydrolysis of AR^+ to produce resorufin (Fig. 21A). With no mesoporous shell, the intermediate AR• could dissociate from Pt NPs and diffuse into the bulk solution before encountering another AR• to go through the disproportionation reaction. On the contrary, the dissociated AR• would be temporarily trapped in nanopores inside the mesoporous shell, thus resulting in high local concentrations of AR• and a fast reaction rate to form the fluorescent product Re.

Super-resolution mapping of the locations, where Re molecules were generated in mesoporous materials of variable pore lengths, was used to experimentally verify the proposed nanoconfinement effect of increasing the local concentration of intermediate species AR• in nanopores. Two super-resolution images were reconstructed (Fig. 21B): mapping of molecular positions where resorufin first formed (down panel, symbol: ●) and through the whole residence time (up panel, symbol: ▲). As shown in the mapping results, both super-resolution images show similar cluster sizes at the same nanopore length. The cluster size matches very well with the physical size of the core–shell particle at all pore lengths (Fig. 21C). Based on these results, we conclude that Re molecules are formed anywhere within the nanopores, rather than just formed on/near the Pt NPs. This can only be explained by the fact that AR• were indeed trapped inside nanopores after dissociation from the Pt NP surface. Considering that the size of core–shell particles is at the nanoscale within the diffraction-limit, the nanometer spatial resolution and turn-over temporal resolution in SMLM are essential to resolve the nanoscale processes involving the intermediate species. Nonetheless, we also discover that the confinement-induced enhancement of catalytic activity will eventually be canceled out, and the catalytic activity will be dominated by the mass transport of reactant molecules.

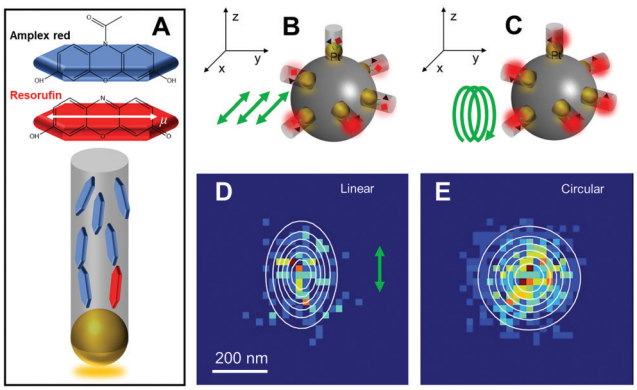

Fig. 20 Unveil molecular orientations in nanopores using SMF polarization microscopy. (A) Dipole moments of AR and Re molecules, and schematic view of molecular arrangement inside nanopores. Single-particle single molecule imaging experiments under linearly polarized excitation (s-pol, B and D) and circularly polarized excitation (c-pol, C and E). Figures are adapted from ref. 116 with permission. Copyright 2019 Nature Publishing Group.

4. Prospects and limitations

Significant progress has been made and exciting results have been obtained in understanding the nanoconfinement effects in porous materials using SMF imaging. Yet, limitations still exist and challenges are to be overcome.

Fluorescent probe molecules are usually several nanometers in size. Nanoconfinement with smaller physical sizes such as micropores (<2 nm) in metal–organic frameworks (MOFs) and interlayer spacing in two-dimensional materials (<1 nm)[120] are not easily accessible. Therefore, chemical dynamics in these types of small nanoconfinement cannot yet be investigated by SMF imaging. Understanding of these types of nanoconfinement is essential for modulating chemistry in a small space and rationally design advanced materials for a variety of applications such as separation, heterogeneous catalysis, energy conversion, and energy storage. On the other hand, SMF imaging of heterogeneous catalysis under nanoconfinement relies on detecting fluorescent product molecules generated in fluorogenic reactions. Many fluorogenic probes have been reported, but the types of chemical reactions or reaction mechanisms that can be studied are still limited. Designing and synthesizing fluorogenic probes that can be correlated to important chemical transformations such as water splitting, oxygen reduction, carbon dioxide reduction, and small alcohol formation are worthy of effort. Furthermore, intermediate species in currently available fluorogenic reactions are commonly nonfluorescent, which makes

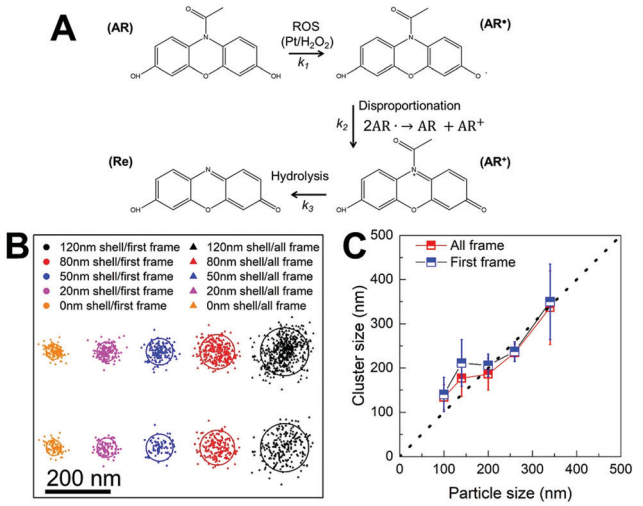

Fig. 21 Cluster analysis of Re positions with and without the mesoporous shell. (A) Reaction mechanism of the oxidation of amplex red to resorufin. (B) Typical cluster distributions of the molecular positions of Re when first detected and during their whole lifetime (all frame) inside nanopores at different pore lengths. The solid line represents the overall average diameter of core–shell nanoparticles. (C) Average cluster sizes from multiple core–shell nanoparticles *versus* the overall diameter of core–shell nanoparticles. Figures are adapted from ref. 116 with permission. Copyright 2019 Nature Publishing Group.

them invisible in fluorescence microscopy. However, these intermediate species are essential for understanding the heterogeneous catalysis under nanoconfinement. For example, tandem catalysis where cascade chemical transformations occur in sequence to generate the desired products in one reactor without the need for separation, purification, and transfer of intermediates produced in each step can be realized with a multifunctional catalyst. Being able to directly monitor each step of chemical transformations, localize where it happens, and determine corresponding kinetics enables one to understand the cause of the better performance of certain catalyst configurations and in turn will largely help in designing highly efficient multifunctional catalysts. One possible strategy would be the design and synthesis of fluorogenic probes that give different fluorescence emission spectra at each step of chemical transformations in tandem catalysis.

The information acquired from SMF imaging on molecular dynamics at the catalyst surface can still be quite limited. Vibrational spectroscopy, such as Raman spectroscopy[121] and attenuated total reflectance Fourier-transform infrared (ATR-FTIR) spectroscopy,[122] is a highly valuable companion to probe the vibrational states of molecules at the interface. Rich molecular fingerprint information from vibrational spectroscopy can reveal the interactions between the catalyst and molecules and the bond breaking/formation in the chemical transformations. Besides molecular dynamics, the structural and electronic properties of the catalyst also significantly affect the catalytic dynamics. For instance, the adsorbate–surface interactions during chemical reactions can induce dynamic surface reconstruction that can vary the surface electronic properties and, in turn, cause oscillatory chemical dynamics. Spectroscopic techniques, such as Raman and photoluminescence (PL), can also be used to monitor the evolution of lattice vibration, electronic band structures and electron density during the catalytic reaction. However, spectroscopic methods still have compatibility issues with the SMF imaging. On the one hand, spectroscopic methods often lack the sensitivity and temporal resolution to monitoring single molecules during a chemical reaction. The ensemble spectroscopic measurement can only provide a limited understanding of molecular behaviors. On the other hand, most spectroscopic methods have insufficient spatial resolution to correlate the molecular behaviors or catalyst properties with heterogeneous chemical dynamics obtained by SMF imaging. Tip-enhanced spectroscopic methods, such as tip-enhanced Raman spectroscopy (TERS),[123–125] tip-enhanced photoluminescence spectroscopy (TEPL),[126,127] and nanoscale infrared spectroscopy (Nano IR),[128,129] have high spatial resolution down to 10 nm[130] in air and sub-nanometer resolution[131] under UHV. They are mostly useful in revealing the molecular behaviors at the surface structures, such as island[132] and edge.[133,134] However, the use of tips (tens of nanometer) in tip-enhanced spectroscopic methods limits the study of molecular behaviors inside porous materials. Hence these techniques can only characterize the molecules confined at the exposure catalyst surface (*e.g.*, defect) but lack the ability to reveal the molecular behaviors in a cavity. Moreover, the much longer acquisition time makes it impractical to monitor catalytic reactions in real time at the nanoscale. Although it is still challenging to combine spectroscopy with SMF imaging where merits from both methods can be obtained, continued efforts, such as the improvement of temporal spatial resolution and sensitivity and the development of new spectroscopic methodologies, are worthy of devotion.

Statistical analysis of single molecule chemical dynamics under nanoconfinement enables one to quantify the heterogeneous mass transport, chemical reaction kinetics, and product dissociation kinetics. Both high localization precision and fast temporary resolution are critical. Despite the efforts and progress made in this field, it is still challenging to acquire both merits in SMF imaging due to the following inherent limitations. (1) The total number of collectable photons is finite, resulting in a shot noise-limited localization precision. (2) Low signal makes the image quality susceptible to interfering background, which is frequently encountered in real-world systems, such as impurities in polymer substrates, and Rayleigh and Raman scattering from porous nanoparticles/microparticles. (3) In order to obtain additional information such as 3D spatial position (*e.g.*, using PSF engineering),[135–138] increased time resolution, and spectroscopic intensity, a limited number of photon signals will be distributed to different channels, which worsens these two problems (low S/N and high background). Currently, typical 2D or 3D localization methods (such as astigmatism,[139] double-helix,[140] defocused,[141] and parallax[142,143]) range from non-linear least squares (NLLS) fitting through the simple correlation coefficient (CC) method[144] to supervised machine learning algorithms (such as maximum likelihood estimation and Bayesian parameter estimation).[145–148] Several strategies can be used to improve the spatial and temporal resolution in SMF imaging. Deep neural

networks (DNNs) have been well recognized for pattern recognition, which abstracts the features from the images at multiple levels by applying various filter matrices for convolution.[149,150] DNNs can be trained to estimate the background patterns[151] and then enable one to remove interference background like that from porous materials, thus obtaining higher localization precision in determining the molecule positions. Another recently developed optical imaging method developed by Hell *et al.*,[152] namely minimal photon fluxes (MINFLUX), is very promising to bring new insights for understanding nanoconfinement at higher spatiotemporal resolution ($\sim$1 nm localization precision and $>$100 times faster).

Porous materials such as metal–organic frameworks (MOFs) and covalent organic frameworks (COFs) have well-defined uniform pore structures, but have rarely been studied using SMF imaging. The MOFs can be used to reach sizes down to the microporous scale ($<$2 nm) in comparison to the industry standard of zeolite catalysts. COFs are recently developed materials with either two-dimensionally aligned or three-dimensional mesopores. The presence of organic linkers in MOFs and COFs is also beneficial to control the chemical environment of the pores, similar to the functionalization of silica pores, but in a more ordered fashion due to the crystalline nature of MOFs and COFs. The advantages of MOFs and COFs are apparent: (i) a versatile and exquisite structural design can be achieved by the judicious selection of preferred topologies, guided by the principles of reticular chemistry;[153,154] (ii) exceptional porosity and highly tunable pore sizes have given rise to an extensive library of crystalline structures;[155,156] (iii) multivariate functionalization allows the incorporation of multiple metals and/or organic ligands into the MOF/COF backbone while preserving their structural integrity;[1,157,158] and (iv) post-synthetic modifications of pre-formed MOFs/COFs have proven to be a potent tool for engineering the environment of the interior pores, as well as modulating the stereoelectronic character of the active sites.[159–161] These distinct features mentioned above have undoubtedly contributed to the extensive study of MOFs/COFs in a plethora of applications in areas ranging from gas storage and separation,[162–167] chemical sensors,[168,169] drug delivery,[13,170] catalysis,[171–173] energy transfer and migration,[174] to energy storage devices.[175,176] Knowledge of the nanoconfinement effects and mass transfer of confined molecules to these well-defined MOFs and COFs is of great interest.

Theoretical studies and modeling of nanoconfinement effects, combined with chemical dynamic data from SMF imaging, are also important directions. Peruchena *et al.* employed density functional theory (DFT) methods and the quantum theory to study the nanoconfinement effects on methylation of benzene in H-ZSM-5 and H-Beta zeolite cavities.[59] They found that zeolites with larger cavities exhibited a higher interaction strength related to adsorption and co-adsorption processes, while smaller zeolites exhibited higher nanoconfinement effects where the stabilization energy is higher in H-ZSM-5 than in H-Beta from an electronic viewpoint. Such theoretical studies and modeling could be readily realized in well-defined porous materials, thus providing complementary insights into chemical dynamics under nanoconfinement.

Conflicts of interest

There are no conflicts to declare.

Acknowledgements

We acknowledge the funding support from the U.S. National Science Foundation (CHE-1609225/1607305).

References

1 H. Xu, J. Gao and D. Jiang, *Nat. Chem.*, 2015, **7**, 905–912.
2 H. Liu, H. Yu, C. Xiong and S. Zhou, *RSC Adv.*, 2015, **5**, 20238–20247.
3 P. Samanta, A. V. Desai, S. Let and S. K. Ghosh, *ACS Sustainable Chem. Eng.*, 2019, **7**, 7456–7478.
4 S. Rapti, D. Sarma, S. A. Diamantis, E. Skliri, G. S. Armatas, A. C. Tsipis, Y. S. Hassan, M. Alkordi, C. D. Malliakas, M. G. Kanatzidis, T. Lazarides, J. C. Plakatouras and M. J. Manos, *J. Mater. Chem. A*, 2017, **5**, 14707–14719.
5 J. T. Cooper, E. M. Peterson and J. M. Harris, *Anal. Chem.*, 2013, **85**, 9363–9370.
6 S. Knoll, T. Rösch and C. Huhn, *Anal. Bioanal. Chem.*, 2020, **412**, 6149–6165.
7 M. Foroutan, S. M. Fatemi and F. Esmaeilian, *Eur. Phys. J. E: Soft Matter Biol. Phys.*, 2017, **40**, 19.
8 W. Lu, Z. Yuan, Y. Zhao, H. Zhang, H. Zhang and X. Li, *Chem. Soc. Rev.*, 2017, **46**, 2199–2236.
9 N. P. Brandon and D. J. Brett, *Philos. Trans. R. Soc., A*, 2006, **364**, 147–159.
10 Suwarno, P. Ngene, A. Nale, T. M. Eggenhuisen, M. Oschatz, J. P. Embs, A. Remhof and P. E. de Jongh, *J. Phys. Chem. C*, 2017, **121**, 4197–4205.
11 S. Chaturvedi, P. N. Dave and N. K. Shah, *J. Saudi Chem. Soc.*, 2012, **16**, 307–325.
12 Y. Zhu, W. Wang, H. Yu and A. Wang, *J. Environ. Sci.*, 2020, **88**, 217–236.
13 Q. Fang, J. Wang, S. Gu, R. B. Kaspar, Z. Zhuang, J. Zheng, H. Guo, S. Qiu and Y. Yan, *J. Am. Chem. Soc.*, 2015, **137**, 8352–8355.
14 T. Lebold, J. Michaelis and C. Brauchle, *Phys. Chem. Chem. Phys.*, 2011, **13**, 5017–5033.
15 A. B. Grommet, M. Feller and R. Klajn, *Nat. Nanotechnol.*, 2020, **15**, 256–271.
16 B. Mitschke, M. Turberg and B. List, *Chem*, 2020, **6**, 2515–2532.
17 S. H. Petrosko, R. Johnson, H. White and C. A. Mirkin, *J. Am. Chem. Soc.*, 2016, **138**, 7443–7445.
18 V. Mouarrawis, R. Plessius, J. I. van der Vlugt and J. N. H. Reek, *Front. Chem.*, 2018, **6**, 623.
19 H. Gao, J. Wang, X. Chen, G. Wang, X. Huang, A. Li and W. Dong, *Nano Energy*, 2018, **53**, 769–797.

20 R. Kumarasinghe, T. Ito and D. A. Higgins, *Anal. Chem.*, 2020, **92**, 1416–1423.
21 R. Kumarasinghe, E. D. Higgins, T. Ito and D. A. Higgins, *J. Phys. Chem. C*, 2016, **120**, 715–723.
22 K. P. F. Janssen, G. De Cremer, R. K. Neely, A. V. Kubarev, J. Van Loon, J. A. Martens, D. E. De Vos, M. B. J. Roeffaers and J. Hofkens, *Chem. Soc. Rev.*, 2013, **43**, 990–1006.
23 P. Chen, X. Zhou, N. M. Andoy, K.-S. Han, E. Choudhary, N. Zou, G. Chen and H. Shen, *Chem. Soc. Rev.*, 2013, **43**, 1107–1117.
24 P. Chen, X. Zhou, H. Shen, N. M. Andoy, E. Choudhary, K.-S. Han, G. Liu and W. Meng, *Chem. Soc. Rev.*, 2010, **39**, 4560–4570.
25 T. Chen, B. Dong, K. Chen, F. Zhao, X. Cheng, C. Ma, S. Lee, P. Zhang, S. H. Kang, J. W. Ha, W. Xu and N. Fang, *Chem. Rev.*, 2017, **117**, 7510–7537.
26 J. J. E. Maris, D. Fu, F. Meirer and B. M. Weckhuysen, *Adsorption*, 2021, **27**, 423–452.
27 J. Michaelis and C. Brauchle, *Chem. Soc. Rev.*, 2010, **39**, 4731–4740.
28 T. Tachikawa and T. Majima, *Chem. Soc. Rev.*, 2010, **39**, 4802–4819.
29 L. Kisley and C. F. Landes, *Anal. Chem.*, 2015, **87**, 83–98.
30 D. A. Higgins, S. C. Park, K.-H. Tran-Ba and T. Ito, *Annu. Rev. Anal. Chem.*, 2015, **8**, 193–216.
31 D. Wang and D. K. Schwartz, *J. Phys. Chem. C*, 2020, **124**, 19880–19891.
32 T. Cordes and S. A. Blum, *Nat. Chem.*, 2013, **5**, 993–999.
33 C. Hellriegel, J. Kirstein and C. Bräuchle, *New J. Phys.*, 2005, **7**, 23.
34 M.-L. I. E. Harwardt, M. S. Dietz, M. Heilemann and T. Wohland, *Biophys. J.*, 2018, **114**, 2432–2443.
35 W. E. Moerner and D. P. Fromm, *Rev. Sci. Instrum.*, 2003, **74**, 3597–3619.
36 E. L. Elson, *Biophys. J.*, 2011, **101**, 2855–2870.
37 R. E. Thompson, D. R. Larson and W. W. Webb, *Biophys. J.*, 2002, **82**, 2775–2783.
38 A. Yildiz, J. N. Forkey, S. A. McKinney, T. Ha, Y. E. Goldman and P. R. Selvin, *Science*, 2003, **300**, 2061.
39 R. J. Barlow, *Statistics: A Guide to the Use of Statistical Methods in the Physical Sciences*, John Wiley & Sons, Chichester, 1989.
40 C. C. Miller and J. Walker, *Proc. R. Soc. London, Ser. A*, 1924, **106**, 724–749.
41 A. von Diezmann, Y. Shechtman and W. E. Moerner, *Chem. Rev.*, 2017, **117**, 7244–7275.
42 L. Zhao, Y. Zhong, Y. Wei, N. Ortiz, F. Chen and G. Wang, *Anal. Chem.*, 2016, **88**, 5122–5130.
43 F. C. Hendriks, F. Meirer, A. V. Kubarev, Z. Ristanović, M. B. J. Roeffaers, E. T. C. Vogt, P. C. A. Bruijnincx and B. M. Weckhuysen, *J. Am. Chem. Soc.*, 2017, **139**, 13632–13635.
44 M. J. Wirth, M. D. Ludes and D. J. Swinton, *Anal. Chem.*, 1999, **71**, 3911–3917.
45 R. L. Hansen and J. M. Harris, *Anal. Chem.*, 1998, **70**, 4247–4256.
46 M. J. Wirth and D. J. Swinton, *J. Phys. Chem. B*, 2001, **105**, 1472–1477.
47 J. J. Newby, M. A. Legg, B. Rogers and M. J. Wirth, *J. Chromatogr. A*, 2011, **1218**, 5131–5135.
48 N. Moitra, S. Ichii, T. Kamei, K. Kanamori, Y. Zhu, K. Takeda, K. Nakanishi and T. Shimada, *J. Am. Chem. Soc.*, 2014, **136**, 11570–11573.
49 E. A. Smith and M. J. Wirth, *J. Chromatogr. A*, 2004, **1060**, 127–134.
50 A. W. Kirkeminde, T. Torres, T. Ito and D. A. Higgins, *J. Phys. Chem. B*, 2011, **115**, 12736–12743.
51 J. Kirstein, B. Platschek, C. Jung, R. Brown, T. Bein and C. Bräuchle, *Nat. Mater.*, 2007, **6**, 303–310.
52 A. Zürner, J. Kirstein, M. Döblinger, C. Bräuchle and T. Bein, *Nature*, 2007, **450**, 705–708.
53 C. Hellriegel, J. Kirstein, C. Bräuchle, V. Latour, T. Pigot, R. Olivier, S. Lacombe, R. Brown, V. Guieu, C. Payrastre, A. Izquierdo and P. Mocho, *J. Phys. Chem. B*, 2004, **108**, 14699–14709.
54 K.-H. Tran-Ba, D. A. Higgins and T. Ito, *Anal. Chem.*, 2015, **87**, 5802–5809.
55 C. Jung, J. Kirstein, B. Platschek, T. Bein, M. Budde, I. Frank, K. Müllen, J. Michaelis and C. Bräuchle, *J. Am. Chem. Soc.*, 2008, **130**, 1638–1648.
56 C. Jung, C. Hellriegel, B. Platschek, D. Wöhrle, T. Bein, J. Michaelis and C. Bräuchle, *J. Am. Chem. Soc.*, 2007, **129**, 5570–5579.
57 T. Lebold, L. A. Mühlstein, J. Blechinger, M. Riederer, H. Amenitsch, R. Köhn, K. Peneva, K. Müllen, J. Michaelis, C. Bräuchle and T. Bein, *Chem. – Eur. J.*, 2009, **15**, 1661–1672.
58 J. Xiao, X. Pan, S. Guo, P. Ren and X. Bao, *J. Am. Chem. Soc.*, 2015, **137**, 477–482.
59 M. F. Zalazar, E. N. Paredes, G. D. Romero Ojeda, N. D. Cabral and N. M. Peruchena, *J. Phys. Chem. C*, 2018, **122**, 3350–3362.
60 A. Bhan and E. Iglesia, *Acc. Chem. Res.*, 2008, **41**, 559–567.
61 R. Gounder and E. Iglesia, *Chem. Commun.*, 2013, **49**, 3491–3509.
62 H. Liu, H. Yu, C. Xiong and S. Zhou, *RSC Adv.*, 2015, **5**, 20238–20247.
63 Z.-A. Qiao, P. Zhang, S.-H. Chai, M. Chi, G. M. Veith, N. C. Gallego, M. Kidder and S. Dai, *J. Am. Chem. Soc.*, 2014, **136**, 11260–11263.
64 C. Wang, X. Lin, Y. Ge, Z. H. Shah, R. Lu and S. Zhang, *RSC Adv.*, 2016, **6**, 102102.
65 K. Mori, T. Urata, S. Okada and H. Yamashita, *Top. Catal.*, 2014, **57**, 1026–1031.
66 M. Tagliazucchi and I. Szleifer, *Mater. Today*, 2015, **18**, 131–142.
67 M. Tagliazucchi and I. Szleifer, *J. Am. Chem. Soc.*, 2015, **137**, 12539–12551.
68 M. Lísal, J. K. Brennan and W. R. Smith, *J. Chem. Phys.*, 2006, **124**, 064712.
69 S. Jakobtorweihen, N. Hansen and F. J. Keil, *J. Chem. Phys.*, 2006, **125**, 224709.

70 A. Malijevský and M. Lísal, *J. Chem. Phys.*, 2009, **130**, 164713.
71 N. Hansen, S. Jakobtorweihen and F. J. Keil, *J. Chem. Phys.*, 2005, **122**, 164705.
72 F. Yang, D. Deng, X. Pan, Q. Fu and X. Bao, *Natl. Sci. Rev.*, 2015, **2**, 183–201.
73 H. Bi, L. Qiao, J.-M. Busnel, B. Liu and H. H. Girault, *J. Proteome Res.*, 2009, **8**, 4685–4692.
74 G. Li, C. Fu, M. B. Oviedo, M. Chen, X. Tian, E. Bekyarova, M. E. Itkis, B. M. Wong, J. Guo and R. C. Haddon, *J. Am. Chem. Soc.*, 2016, **138**, 40–43.
75 H. Zhao, S. Sen, T. Udayabhaskararao, M. Sawczyk, K. Kučanda, D. Manna, P. K. Kundu, J.-W. Lee, P. Král and R. Klajn, *Nat. Nanotechnol.*, 2016, **11**, 82–88.
76 B. Dong, X. Yang, S. Zhu, D. C. Bassham and N. Fang, *Sci. Rep.*, 2015, **5**, 15694.
77 K. Xu, H. P. Babcock and X. Zhuang, *Nat. Methods*, 2012, **9**, 185–188.
78 A. Sharonov and R. M. Hochstrasser, *Proc. Natl. Acad. Sci. U. S. A.*, 2006, **103**, 18911.
79 F. C. Hendriks, S. Mohammadian, Z. Ristanović, S. Kalirai, F. Meirer, E. T. C. Vogt, P. C. A. Bruijnincx, H. C. Gerritsen and B. M. Weckhuysen, *Angew. Chem., Int. Ed.*, 2018, **57**, 257–261.
80 J. Van Loon, A. V. Kubarev and M. B. J. Roeffaers, *ChemNanoMat*, 2018, **4**, 6–14.
81 K.-I. Setsukinai, Y. Urano, K. Kakinuma, H. J. Majima and T. Nagano, *J. Biol. Chem.*, 2003, **278**, 3170–3175.
82 W. Jakubowski and G. Bartosz, *Cell Biol. Int.*, 2000, **24**, 757–760.
83 T. Tachikawa, N. Wang, S. Yamashita, S.-C. Cui and T. Majima, *Angew. Chem., Int. Ed.*, 2010, **49**, 8593–8597.
84 C. Bueno, M. L. Villegas, S. G. Bertolotti, C. M. Previtali, M. G. Neumann and M. V. Encinas, *Photochem. Photobiol.*, 2002, **76**, 385–390.
85 S. J. Lord, N. R. Conley, H.-L. D. Lee, R. Samuel, N. Liu, R. J. Twieg and W. E. Moerner, *J. Am. Chem. Soc.*, 2008, **130**, 9204–9205.
86 S. J. Lord, N. R. Conley, H.-L. D. Lee, S. Y. Nishimura, A. K. Pomerantz, K. A. Willets, Z. Lu, H. Wang, N. Liu, R. Samuel, R. Weber, A. Semyonov, M. He, R. J. Twieg and W. E. Moerner, *ChemPhysChem*, 2009, **10**, 55–65.
87 P. Shieh, V. T. Dien, B. J. Beahm, J. M. Castellano, T. Wyss-Coray and C. R. Bertozzi, *J. Am. Chem. Soc.*, 2015, **137**, 7145–7151.
88 P. Shieh, M. J. Hangauer and C. R. Bertozzi, *J. Am. Chem. Soc.*, 2012, **134**, 17428–17431.
89 P. Shieh, M. S. Siegrist, A. J. Cullen and C. R. Bertozzi, *Proc. Natl. Acad. Sci. U. S. A.*, 2014, **111**, 5456.
90 C. Le Droumaguet, C. Wang and Q. Wang, *Chem. Soc. Rev.*, 2010, **39**, 1233–1239.
91 J. C. Park, E. Heo, A. Kim, M. Kim, K. H. Park and H. Song, *J. Phys. Chem. C*, 2011, **115**, 15772–15777.
92 M. Kim, J. C. Park, A. Kim, K. H. Park and H. Song, *Langmuir*, 2012, **28**, 6441–6447.
93 N. T. S. Phan, M. Van Der Sluys and C. W. Jones, *Adv. Synth. Catal.*, 2006, **348**, 609–679.
94 T. Rohand, W. Qin, N. Boens and W. Dehaen, *Eur. J. Org. Chem.*, 2006, 4658–4663.
95 X. Zhou, N. M. Andoy, G. Liu, E. Choudhary, K.-S. Han, H. Shen and P. Chen, *Nat. Nanotechnol.*, 2012, **7**, 237–241.
96 J. W. Ha, T. P. A. Ruberu, R. Han, B. Dong, J. Vela and N. Fang, *J. Am. Chem. Soc.*, 2014, **136**, 1398–1408.
97 T. Tachikawa and T. Majima, *J. Am. Chem. Soc.*, 2009, **131**, 8485–8495.
98 T. Tachikawa, S. Yamashita and T. Majima, *J. Am. Chem. Soc.*, 2011, **133**, 7197–7204.
99 M. B. J. Roeffaers, B. F. Sels, H. Uji-i, F. C. De Schryver, P. A. Jacobs, D. E. De Vos and J. Hofkens, *Nature*, 2006, **439**, 572–575.
100 M. J. K. Ow, J. J. Ng, J. X. Yong, B. Y. L. Quek, E. K. L. Yeow and Z. Zhang, *ACS Appl. Nano Mater.*, 2020, **3**, 3163–3167.
101 M. Shen, T. Ding, S. T. Hartman, F. Wang, C. Krucylak, Z. Wang, C. Tan, B. Yin, R. Mishra, M. D. Lew and B. Sadtler, *ACS Catal.*, 2020, **10**, 2088–2099.
102 Z. Ristanović, M. M. Kerssens, A. V. Kubarev, F. C. Hendriks, P. Dedecker, J. Hofkens, M. B. J. Roeffaers and B. M. Weckhuysen, *Angew. Chem., Int. Ed.*, 2015, **54**, 1836–1840.
103 W. Xu, J. S. Kong, Y.-T. E. Yeh and P. Chen, *Nat. Mater.*, 2008, **7**, 992.
104 H. P. Lu, L. Xun and X. S. Xie, *Science*, 1998, **282**, 1877–1882.
105 Z. Ristanović, A. D. Chowdhury, R. Y. Brogaard, K. Houben, M. Baldus, J. Hofkens, M. B. J. Roeffaers and B. M. Weckhuysen, *J. Am. Chem. Soc.*, 2018, **140**, 14195–14205.
106 K. Lin, P. P. Pescarmona, H. Vandepitte, D. Liang, G. Van Tendeloo and P. A. Jacobs, *J. Catal.*, 2008, **254**, 64–70.
107 K. Lin, P. P. Pescarmona, K. Houthoofd, D. Liang, G. Van Tendeloo and P. A. Jacobs, *J. Catal.*, 2009, **263**, 75–82.
108 G. De Cremer, M. B. J. Roeffaers, E. Bartholomeeusen, K. Lin, P. Dedecker, P. P. Pescarmona, P. A. Jacobs, D. E. De Vos, J. Hofkens and B. F. Sels, *Angew. Chem., Int. Ed.*, 2010, **122**, 920–923.
109 M. B. J. Roeffaers, G. De Cremer, J. Libeert, R. Ameloot, P. Dedecker, A.-J. Bons, M. Bückins, J. A. Martens, B. F. Sels, D. E. De Vos and J. Hofkens, *Angew. Chem., Int. Ed.*, 2009, **121**, 9449–9453.
110 Z. Ristanović, J. P. Hofmann, G. De Cremer, A. V. Kubarev, M. Rohnke, F. Meirer, J. Hofkens, M. B. J. Roeffaers and B. M. Weckhuysen, *J. Am. Chem. Soc.*, 2015, **137**, 6559–6568.
111 Z. Ristanović, A. V. Kubarev, J. Hofkens, M. B. J. Roeffaers and B. M. Weckhuysen, *J. Am. Chem. Soc.*, 2016, **138**, 13586–13596.
112 A. V. Kubarev, K. P. F. Janssen and M. B. J. Roeffaers, *ChemCatChem*, 2015, **7**, 3646–3650.
113 A. Garcia Iv, S. J. Saluga, D. J. Dibble, P. A. López, N. Saito and S. A. Blum, *Angew. Chem., Int. Ed.*, 2020, **133**, 1574–1579.

114 B. Dong, Y. Pei, F. Zhao, T. W. Goh, Z. Qi, C. Xiao, K. Chen, W. Huang and N. Fang, *Nat. Catal.*, 2018, **1**, 135–140.
115 Y. Cao and S. H. Kang, *Bull. Korean Chem. Soc.*, 2019, **40**, 14–19.
116 B. Dong, Y. Pei, N. Mansour, X. Lu, K. Yang, W. Huang and N. Fang, *Nat. Commun.*, 2019, **10**, 4815.
117 I. K. Mbaraka and B. H. Shanks, *J. Catal.*, 2005, **229**, 365–373.
118 B. Dong, N. Mansour, Y. Pei, Z. Wang, T. Huang, S. L. Filbrun, M. Chen, X. Cheng, M. Pruski, W. Huang and N. Fang, *J. Am. Chem. Soc.*, 2020, **142**, 13305–13309.
119 R. Serra-Maia, M. Bellier, S. Chastka, K. Tranhuu, A. Subowo, J. D. Rimstidt, P. M. Usov, A. J. Morris and F. M. Michel, *ACS Appl. Mater. Interfaces*, 2018, **10**, 21224–21234.
120 Q. Fu and X. Bao, *Chem. Soc. Rev.*, 2017, **46**, 1842–1874.
121 T. Hartman, C. S. Wondergem, N. Kumar, A. van den Berg and B. M. Weckhuysen, *J. Phys. Chem. Lett.*, 2016, **7**, 1570–1584.
122 J.-M. Andanson and A. Baiker, *Chem. Soc. Rev.*, 2010, **39**, 4571–4584.
123 X. Wang, S.-C. Huang, T.-X. Huang, H.-S. Su, J.-H. Zhong, Z.-C. Zeng, M.-H. Li and B. Ren, *Chem. Soc. Rev.*, 2017, **46**, 4020–4041.
124 T.-X. Huang, X. Cong, S.-S. Wu, K.-Q. Lin, X. Yao, Y.-H. He, J.-B. Wu, Y.-F. Bao, S.-C. Huang, X. Wang, P.-H. Tan and B. Ren, *Nat. Commun.*, 2019, **10**, 5544.
125 Z.-C. Zeng, S.-C. Huang, D.-Y. Wu, L.-Y. Meng, M.-H. Li, T.-X. Huang, J.-H. Zhong, X. Wang, Z.-L. Yang and B. Ren, *J. Am. Chem. Soc.*, 2015, **137**, 11928–11931.
126 K.-D. Park, O. Khatib, V. Kravtsov, G. Clark, X. Xu and M. B. Raschke, *Nano Lett.*, 2016, **16**, 2621–2627.
127 C. Tang, S. Jia, W. Chen, J. Lou and D. V. Voronine, 2017, arXiv preprint arXiv:1704.02396.
128 F. Huth, A. Govyadinov, S. Amarie, W. Nuansing, F. Keilmann and R. Hillenbrand, *Nano Lett.*, 2012, **12**, 3973–3978.
129 Z. Fei, A. S. Rodin, G. O. Andreev, W. Bao, A. S. McLeod, M. Wagner, L. M. Zhang, Z. Zhao, M. Thiemens, G. Dominguez, M. M. Fogler, A. H. C. Neto, C. N. Lau, F. Keilmann and D. N. Basov, *Nature*, 2012, **487**, 82–85.
130 E. M. van Schrojenstein Lantman, T. Deckert-Gaudig, A. J. G. Mank, V. Deckert and B. M. Weckhuysen, *Nat. Nanotechnol.*, 2012, **7**, 583–586.
131 R. Zhang, Y. Zhang, Z. C. Dong, S. Jiang, C. Zhang, L. G. Chen, L. Zhang, Y. Liao, J. Aizpurua, Y. Luo, J. L. Yang and J. G. Hou, *Nature*, 2013, **498**, 82–86.
132 G. Delen, M. Monai, F. Meirer and B. M. Weckhuysen, *Angew. Chem., Int. Ed.*, 2021, **60**, 1620–1624.
133 J.-H. Zhong, X. Jin, L. Meng, X. Wang, H.-S. Su, Z.-L. Yang, C. T. Williams and B. Ren, *Nat. Nanotechnol.*, 2017, **12**, 132–136.
134 C.-Y. Wu, W. J. Wolf, Y. Levartovsky, H. A. Bechtel, M. C. Martin, F. D. Toste and E. Gross, *Nature*, 2017, **541**, 511–515.
135 S. R. P. Pavani, M. A. Thompson, J. S. Biteen, S. J. Lord, N. Liu, R. J. Twieg, R. Piestun and W. E. Moerner, *Proc. Natl. Acad. Sci. U. S. A.*, 2009, **106**, 2995–2999.
136 M. J. Rust, M. Bates and X. W. Zhuang, *Nat. Methods*, 2006, **3**, 793–795.
137 K. C. Chen, Y. Gu, W. Sun, B. Dong, G. F. Wang, X. X. Fan, T. Xia and N. Fang, *Nat. Commun.*, 2017, **8**, 887.
138 L. Y. Zhao, Y. N. Zhong, Y. L. Wei, N. Ortiz, F. Chen and G. F. Wang, *Anal. Chem.*, 2016, **88**, 5122–5130.
139 B. Huang, W. Wang, M. Bates and X. Zhuang, *Science*, 2008, **319**, 810.
140 S. R. P. Pavani, M. A. Thompson, J. S. Biteen, S. J. Lord, N. Liu, R. J. Twieg, R. Piestun and W. E. Moerner, *Proc. Natl. Acad. Sci. U. S. A.*, 2009, **106**, 2995–2999.
141 E. Toprak, H. Balci, B. H. Blehm and P. R. Selvin, *Nano Lett.*, 2007, **7**, 2043–2045.
142 Y. Sun, J. D. McKenna, J. M. Murray, E. M. Ostap and Y. E. Goldman, *Nano Lett.*, 2009, **9**, 2676–2682.
143 K. Chen, Y. Gu, W. Sun, D. Bin, G. Wang, X. Fan, T. Xia and N. Fang, *Nat. Commun.*, 2017, **8**, 887.
144 M. P. Sheetz, S. Turney, H. Qian and E. L. Elson, *Nature*, 1989, **340**, 284–288.
145 A. Small and S. Stahlheber, *Nat. Methods*, 2014, **11**, 267–279.
146 T. Mitchell, *Machine Learning*, McGraw-Hill Higher Education, New York, 1997.
147 T. M. Mitchell, *Mach. Learn.*, 2006, **21**, 17.
148 M. Collins, R. E. Schapire and Y. Singer, *Mach. Learn.*, 2002, **48**, 253–285.
149 K. Lenc and A. Vedaldi, presented in part at the CVPR, 2015.
150 Y. LeCun, presented in part at the ECCV Workshops and demonstrations, Springer, Berlin Heidelberg, 2012.
151 L. Möckl, A. R. Roy, P. N. Petrov and W. E. Moerner, *Proc. Natl. Acad. Sci. U. S. A.*, 2020, **117**, 60.
152 F. Balzarotti, Y. Eilers, K. C. Gwosch, A. H. Gynnå, V. Westphal, F. D. Stefani, J. Elf and S. W. Hell, *Science*, 2017, **355**, 606.
153 C. S. Diercks and O. M. Yaghi, *Science*, 2017, 355.
154 M. O'Keeffe and O. M. Yaghi, *Chem. Rev.*, 2011, **112**, 675–702.
155 S. Kitagawa, *Chem. Soc. Rev.*, 2014, **43**, 5415–5418.
156 N. Huang, P. Wang and D. Jiang, *Nat. Rev. Mater.*, 2016, **1**, 16068.
157 Y.-B. Zhang, H. Furukawa, N. Ko, W. Nie, H. J. Park, S. Okajima, K. E. Cordova, H. Deng, J. Kim and O. M. Yaghi, *J. Am. Chem. Soc.*, 2015, **137**, 2641–2650.
158 H. Deng, C. J. Doonan, H. Furukawa, R. B. Ferreira, J. Towne, C. B. Knobler, B. Wang and O. M. Yaghi, *Science*, 2010, **327**, 846–850.
159 Z. Wang and S. M. Cohen, *Chem. Soc. Rev.*, 2009, **38**, 1315–1329.
160 S. M. Cohen, *Chem. Rev.*, 2012, **112**, 970–1000.
161 P. Deria, J. E. Mondloch, O. Karagiaridi, W. Bury, J. T. Hupp and O. K. Farha, *Chem. Soc. Rev.*, 2014, **43**, 5896–5912.
162 K. Sumida, D. L. Rogow, J. A. Mason, T. M. McDonald, E. D. Bloch, Z. R. Herm, T.-H. Bae and J. R. Long, *Chem. Rev.*, 2012, **112**, 724–781.
163 L. J. Murray, M. Dincă and J. R. Long, *Chem. Soc. Rev.*, 2009, **38**, 1294–1314.
164 J.-R. Li, J. Sculley and H.-C. Zhou, *Chem. Rev.*, 2012, **112**, 869–932.

165 J. B. DeCoste and G. W. Peterson, *Chem. Rev.*, 2014, **114**, 5695–5727.
166 Y. Zeng, R. Zou and Y. Zhao, *Adv. Mater.*, 2016, **28**, 2855–2873.
167 J. T. Yu, Z. Chen, J. L. Sun, Z. T. Huang and Q. Y. Zheng, *J. Mater. Chem.*, 2012, **22**, 5369–5373.
168 L. E. Kreno, K. Leong, O. K. Farha, M. Allendorf, R. P. Van Duyne and J. T. Hupp, *Chem. Rev.*, 2012, **112**, 1105–1125.
169 M. R. Rao, Y. Fang, S. De Feyter and D. F. Perepichka, *J. Am. Chem. Soc.*, 2017, **139**, 2421–2427.
170 C.-Y. Sun, C. Qin, X.-L. Wang and Z.-M. Su, *Expert Opin. Drug Delivery*, 2013, **10**, 89–101.
171 T. Zhang and W. Lin, *Chem. Soc. Rev.*, 2014, **43**, 5982–5993.
172 S.-Y. Ding, J. Gao, Y. Zhang, W.-G. Song, C.-Y. Su and W. Wang, *J. Am. Chem. Soc.*, 2011, **133**, 19816.
173 X. Han, Q. Xia, J. Huang, Y. Liu, C. Tan and Y. Cui, *J. Am. Chem. Soc.*, 2017, **139**, 8693–8697.
174 S. Wan, J. Guo, J. Kim, H. Ihee and D. L. Jiang, *Angew. Chem., Int. Ed.*, 2008, **47**, 8826–8830.
175 K. M. Choi, H. M. Jeong, J. H. Park, Y.-B. Zhang, J. K. Kang and O. M. Yaghi, *ACS Nano*, 2014, **8**, 7451–7457.
176 H. Bildirir, V. G. Gregoriou, A. Avgeropoulos, U. Scherf and C. L. Chochos, *Mater. Horiz.*, 2017, **4**, 546–556.

